





# Regenerating aged bone marrow via a nitric oxide nanopump

Received: 15 January 2025

Accepted: 17 June 2025

Published online: 01 July 2025



Ke Li<sup>1,2,3,4</sup>, Sihan Hu<sup>1,3,4</sup>, Hanwen Li<sup>2,3,4</sup>, Wenzheng Lin<sup>1,2,3</sup>, Duoyi Zhao<sup>1,2,3</sup>, Zhuobin Xu<sup>1,3</sup>, Chun Pan<sup>1,3</sup>, Huihui Wang<sup>1,3</sup> , Dandan Li<sup>1,3</sup>, Jingjing Liu<sup>1,3</sup>  & Hao Chen<sup>1,2,3</sup>  

Resident leptin-receptor-expressing (LepR<sup>+</sup>) cells senesce in the aged bone marrow impairs the regenerative capacity of osteo- and other lineages of cells. In this study, a LepR<sup>+</sup> cell-targeting nitric oxide (NO) nanopump with in vivo self-controlled turn-on ability was constructed to rejuvenate the LepR<sup>+</sup> cells in the aged bone marrow. The nanopump co-entrapped hydrophobic chemiluminescence substrate and NO donor into the matrix of amphiphilic polymer through a nanoprecipitation process. The chemiluminescence substrate in the NO nanopump automatically reacts with the accumulated H<sub>2</sub>O<sub>2</sub> in the aged bone marrow and then directly transfers the chemical energy to the NO donor to induce in situ NO release. The NO produced in situ within the aged bone marrow triggered the regeneration of the osteoblastic and the other niches in vivo through activating the glycolysis signaling in the senescent LepR<sup>+</sup> cells. Conclusively, the constructed NO nanopump is a promising tool to counter aging-induced bone marrow disorders.

Aged skeletal stem cells (SSCs) generate inflammatory degenerative niches in the bone marrow (BM) by secreting high levels of pro-inflammatory and pro-resorptive cytokines, leading to senescence-associated BM collapse manifested by myeloid skewing in haematopoietic stem cells (HSCs), reduced vascular regeneration, inhibited neural sprouting, and severe bone loss<sup>1</sup>. Recent studies have indicated that LepR-expressing (LepR<sup>+</sup>) cells constitute a major population of SSCs in adulthood<sup>2,3</sup>. LepR<sup>+</sup> cells that reside in the BM are specialized multicellular units that maintain the ability to regenerate bone<sup>2,4–6</sup>. Fate mapping has indicated that LepR<sup>+</sup> cells emerge in the postnatal BM and represent the primary source of bone and adipocytes in the adult BM<sup>2,3</sup>. Unexpectedly, LepR<sup>+</sup> cells in the central BM of adult mice help maintain HSCs function and vascular, lymphatic vessel regeneration by secreting HSCs-supporting factors (including stem cell factor, SCF) and vascular endothelial growth factor-C (VEGF-C)<sup>6–10</sup>. The nerve growth factor (NGF) produced by LepR<sup>+</sup> cells has been shown to promote neural sprouting in the adult BM<sup>4</sup>. However, the key HSCs-supporting factors derived from LepR<sup>+</sup> cells markedly decrease with age, resulting in BM exhaustion<sup>8,9</sup>. Therefore, LepR<sup>+</sup> cells are believed

to play critical roles in maintaining the homeostasis of the BM. Notably, our observations and previous reports revealed that the accumulation of senescent LepR<sup>+</sup> cells occurred in the BM microenvironment of aged mice<sup>11</sup>, suggesting that senescent LepR<sup>+</sup> cells may not only lead to an impaired osteoblast lineage but also disrupt overall BM homeostasis under aged conditions. Considering that the maintenance of BM homeostasis largely depends on viable LepR<sup>+</sup> cells, it is necessary to explore approaches to rejuvenate senescent LepR<sup>+</sup> cells to reestablish homeostasis of aging-induced BM collapse.

Nitric oxide (NO) is an endogenous gaseous transmitter that has been focused by intense research since its discovery. NO is recognized for its involvement in various biometabolic processes, such as vasodilation, platelet activity, neurotransmission, bone regeneration, and the regulation of immunological and metabolic systems<sup>12–14</sup>. Moreover, NO plays an active role in host defense and anti-inflammatory processes, conferring a protective effect on the host<sup>13</sup>. Hence, in regard to the aged BM microenvironment exhibits regenerative failure and inflammatory infiltration in HSCs, blood vessels, nerves and bone, there might be considerable potential for NO to function in the

<sup>1</sup>Institute of Translational Medicine, Medical College, Yangzhou University, Yangzhou, China. <sup>2</sup>Department of Orthopedic, Affiliated Hospital of Yangzhou University, Yangzhou, China. <sup>3</sup>The Key Laboratory of the Jiangsu Higher Education Institutions for Nucleic Acid & Cell Fate Regulation, Yangzhou, China.

<sup>4</sup>These authors contributed equally: Ke Li, Sihan Hu, Hanwen Li. ✉ e-mail: [jjliu0105@yzu.edu.cn](mailto:jjliu0105@yzu.edu.cn); [hchen2020@yzu.edu.cn](mailto:hchen2020@yzu.edu.cn)

regeneration of aging-induced BM collapse. However, the direct delivery of NO in the form of gas in bone tissue is challenging due to its transitory half-life (less than 5 s) and short diffusion radius (40–200  $\mu\text{m}$ )<sup>15–17</sup>. The delivery of exogenous NO donors may be an alternative strategy to achieve effective NO delivery. An exogenous NO donor, isosorbide mononitrate, has been shown to improve vascular endothelial cell and osteoblast function in elderly patients<sup>18,19</sup>. In addition, the use of diethylenetriamine diazenium diolate (NONOate), another NO donor, has also been attempted to prevent bone loss and wound infection<sup>20,21</sup>. However, once the agent is discontinued, bone loss occurs rapidly due to the rapid removal of NONOate from the body. To overcome this challenge, an injectable microparticle system was synthesized to encapsulate NONOate, which actively traps NO bubbles and extends the half-life of NO<sup>22</sup>. However, this regimen is largely dependent on frequent subcutaneous administration, and its poor ability to target bone tissue warrants further improvement. Alternatively, a bone-targeted photosensitive NO-generating nanoplatfrom that responds to near-infrared (NIR) light was constructed<sup>16</sup>. In this design, the lanthanide ion ( $\text{Ln}^{3+}$ )-doped nanoplatfrom is able to convert illuminated NIR light (808 nm) into UV/blue light, causing in situ NO release from the NO donor (N,N'-di-sec-butyl-N,N'-dinitroso-p-phenylenediamine (BNN6)), which reduces bone loss. However, the poor permeability and low efficiency of excitation light (even in the near-infrared region) severely hinder its application in deep bone tissue<sup>23</sup>.

In this study, we observed that aging-induced BM collapse is possibly due to the senescence of  $\text{LepR}^+$  cells resulting from insufficient NO supply. Hence, we developed an efficient strategy for in situ NO release by co-encapsulating bis(2-carboxypentoxo-3,5,6-trichlorophenyl) oxalate (CPPO) and BNN6 via a nanoprecipitation method (CB-NPs). Specifically, instead of relying on the complexity of the conversion and cascade in traditional NO delivery systems, the CPPO in the NO nanopump automatically reacts with  $\text{H}_2\text{O}_2$  and directly transfers energy to the NO donor, achieving in situ stimulus-responsive controlled NO release. Moreover, given the short lifetime of NO, the addition of soybean oil slowed the reaction between CPPO and  $\text{H}_2\text{O}_2$ , which significantly prolonged the half-life of NO. Since NO nanopumps targeting  $\text{LepR}^+$  cells are required to achieve intracellular NO release, the  $\text{LepR}$  antibody was conjugated onto the surface of CB-NPs (CB-LepR) to arm the nanopump with a  $\text{LepR}^+$  cell-targeting ability (Fig. 1).

## Results

### $\text{LepR}^+$ cells senescence, $\text{H}_2\text{O}_2$ accumulation and NO reduction occur in aged BM

Deletion of argininosuccinate lyase (ASL) reduces NO production within cells<sup>24,25</sup>. Notably,  $\text{LepR}^+$  cells in aged mice presented considerably lower levels of ASL as compared to the young mice (Fig. 2A). As NO has anti-aging potential, the expression of P21,  $\gamma\text{-H2AX}$  and IL-6 in  $\text{LepR}^+$  cells within the femurs of aged mice were evaluated. The results showed the expression of P21,  $\gamma\text{-H2AX}$  and IL-6 was significantly increased in the  $\text{LepR}^+$  cells within the femurs of aged mice, indicating that aging induced a marked increase in  $\text{LepR}^+$  cells senescence in the BM (Fig. 2A, B, Supplementary Fig. 1A, B). Moreover, deteriorated regeneration of bone, blood vessels, lymphatic vessels, and nerve fibers was also observed in the aged BM, suggesting that the collapsed BM under aged conditions was most likely induced by  $\text{LepR}^+$  cells senescence with age (Fig. 2A–D). Evidence that HSCs with myeloid-biased outputs (my-HSCs, Lineage Sca-1<sup>+</sup>c-Kit<sup>+</sup> (LSK)CD48<sup>+</sup>CD150<sup>high</sup> HSCs) are strongly associated with senescence has led to further evaluation of my-HSCs in the BM<sup>26</sup>. A significant increase in my-HSCs and a considerable decrease in  $\text{LepR}^+$  cell-derived factors that maintain the function of HSCs (including SCF, encoded by *Kitl* gene) were observed in aged BM (Fig. 2E–G), providing further evidence that senescent  $\text{LepR}^+$  cells facilitate aged BM collapse.

Aging is typically accompanied by increased oxidative stress<sup>27</sup>. To investigate the changes in  $\text{H}_2\text{O}_2$  levels in vivo, a  $\text{H}_2\text{O}_2$  probe was injected into the femoral marrow cavities of young and aged mice. As shown in Fig. 2H, I, the fluorescence of the  $\text{H}_2\text{O}_2$  probe increased significantly in the femurs of aged mice, indicating the accumulation of  $\text{H}_2\text{O}_2$  in the femoral marrow cavity during aging. The concentration of  $\text{H}_2\text{O}_2$  in the aged BM was subsequently evaluated. Compared with that in young mice, the amount of  $\text{H}_2\text{O}_2$  in the marrow cavity was approximately eight-fold greater in aged mice (Fig. 2J). These results revealed that aging BM exhibited a decrease in ASL expression and NO production, and an increase in  $\text{H}_2\text{O}_2$  accumulation and  $\text{LepR}^+$  cellular senescence. Hence, the aberrant accumulation of  $\text{H}_2\text{O}_2$  sets the stage for the chemical excitation of NO donors via specific reactions between  $\text{H}_2\text{O}_2$  and peroxyoxalate.

### Construction and characterization of NO nanopumps

The key to achieving in vivo chemical excitation of BNN6 to produce NO is the construction of CB-NPs through the nanoprecipitation method (Fig. 3A). The drug-loading content (DLC) of the CB-NPs was 9.5% for CPPO and 5.9% for BNN6 (Supplementary Fig. 2A–D). The CB-NPs were then modified with a  $\text{LepR}$  antibody to obtain CB-LepR. Both CB-NPs and CB-LepR exhibited a spherical morphology with mean diameters of  $118.3 \pm 10.5$  and  $125.9 \pm 0.25$  nm, respectively (Fig. 3B–C). Both nanoparticles remained the same size in 10% fetal bovine serum for 3 days, demonstrating ideal stability (Fig. 3D). The presence of BNN6, CPPO, and DSPE-PEG-MAL in CB-NPs was subsequently verified via high-performance liquid chromatography (HPLC) and elemental mapping. As shown in Fig. 3E and Supplementary Fig. 2E, the characteristic peaks of CPPO and BNN6 in CB-NPs co-localized with their individual peaks, and elemental mapping revealed that the Cl of CPPO and S of DSPE-PEG-MAL coexisted within the CB-LepR nanoparticles, indicating that BNN6, CPPO, and DSPE-PEG-MAL were successfully encapsulated in the nanoparticles.

Upon exposure of CB-NPs to  $\text{H}_2\text{O}_2$ , the energetic intermediate 1,2-dioxidone (DOD) is generated by the reaction of CPPO with  $\text{H}_2\text{O}_2$ <sup>28</sup>. With the proper alignment of the energy levels between the highest occupied molecular orbital (HOMO) of BNN6 and the lowest unoccupied molecular orbital (LUMO) of DOD, it is possible to directly excite BNN6 (Fig. 3A). According to Gaussian 09 calculations, the HOMO energy level of BNN6 and the LUMO energy level of DOD were  $-6.22$  and  $-3.33$  eV, respectively (Fig. 3F). The relatively small energy interval of 2.89 eV is sufficient for the direct chemiexcitation of BNN6, resulting in the generation of NO (Fig. 3G). Through examination of the BNN6 content alteration in CB-LepR following its reaction with  $\text{H}_2\text{O}_2$  via liquid chromatography–mass spectrometry, we observed a decrease in the ionic intensity of BNN6 ( $m/z = 278.35$ ) within the NO nanopumps from  $6.27 \times 10^5$  to  $3 \times 10^5$  after the reaction with  $\text{H}_2\text{O}_2$  (Supplementary Fig. 3A, B). Additionally, the NO release behavior of CB-LepR after reaction with  $\text{H}_2\text{O}_2$  was investigated. As shown in Fig. 3H, NO was cumulatively released from CB-LepR in the presence of  $\text{H}_2\text{O}_2$ . All the results indicated that the interactions among CPPO,  $\text{H}_2\text{O}_2$ , and BNN6 occurred through the generation of the energetic intermediate DOD. By further analyzing the NO release results, we found that under highly excessive CB-LepR, the generation rate of NO on day 1 ( $r_1$ :  $\mu\text{M} \cdot \text{d}^{-1}$ ) was proportional to the square root of the  $\text{H}_2\text{O}_2$  concentration ( $\text{cH}_2\text{O}_2$ ) ( $\mu\text{M}$ ) ( $r_1 = 0.8851\sqrt{\text{cH}_2\text{O}_2} - 1.16$ ,  $R^2 = 0.99$ ). Furthermore, under a certain concentration of  $\text{H}_2\text{O}_2$ , the generation rate of NO within 10 days is inversely proportional to the square of the NO concentration on that day. After 10 days, the generation rate of NO remained low because the reaction reached equilibrium (Supplementary Fig. 4A–E). Thus, the chemical kinetics results suggested that with the given  $\text{H}_2\text{O}_2$  concentration (6.25–50  $\mu\text{M}$ ), the NO release from excess CB-LepR on each day (1–14 days) could be quantitatively calculated.

Next, the biocompatibility of CB-LepR was examined. Following the identification of the maximum safe concentration of  $\text{H}_2\text{O}_2$  for a

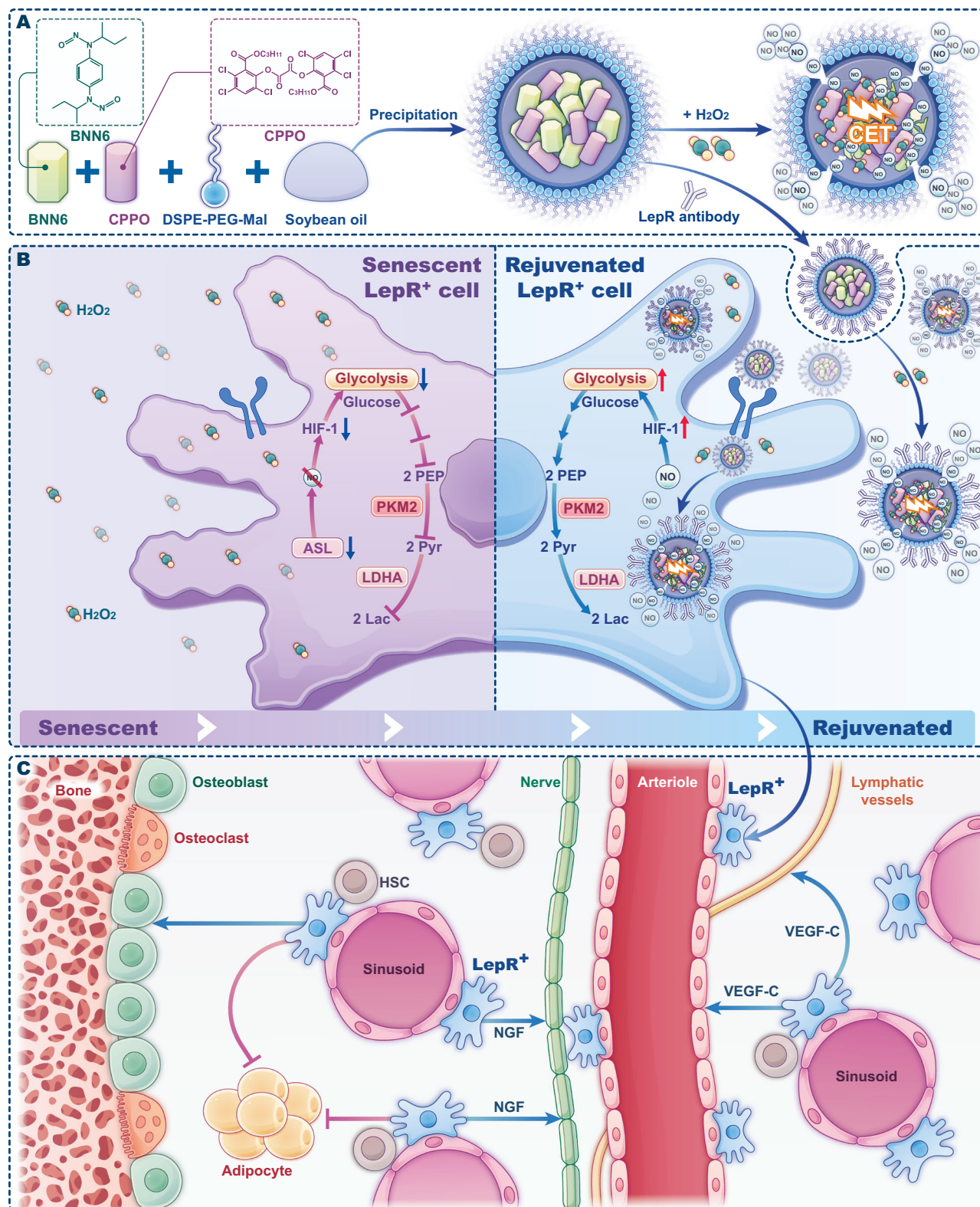


**Fig. 1 | The process to re-establish homeostasis in aging-induced bone marrow collapse via the rejuvenation of senescent LepR<sup>+</sup> cells with the NO nanopump. A** Construction of NO nanopump targeting LepR<sup>+</sup> cells. **B** The NO nanopump scavenges the accumulated H<sub>2</sub>O<sub>2</sub> in the aged BM, followed by the production of 1,2-dioxetanedione (DOD), the high-energy intermediate to directly excite the NO

donor, causing in situ NO release to rejuvenate the senescent LepR<sup>+</sup> cells by activating glycolysis signaling. **C** Rejuvenation of senescent LepR<sup>+</sup> cells with the NO nanopump reestablished homeostasis via regeneration of HSCs, blood vessels, lymphatic vessels, and nerve fibers in aged BM.



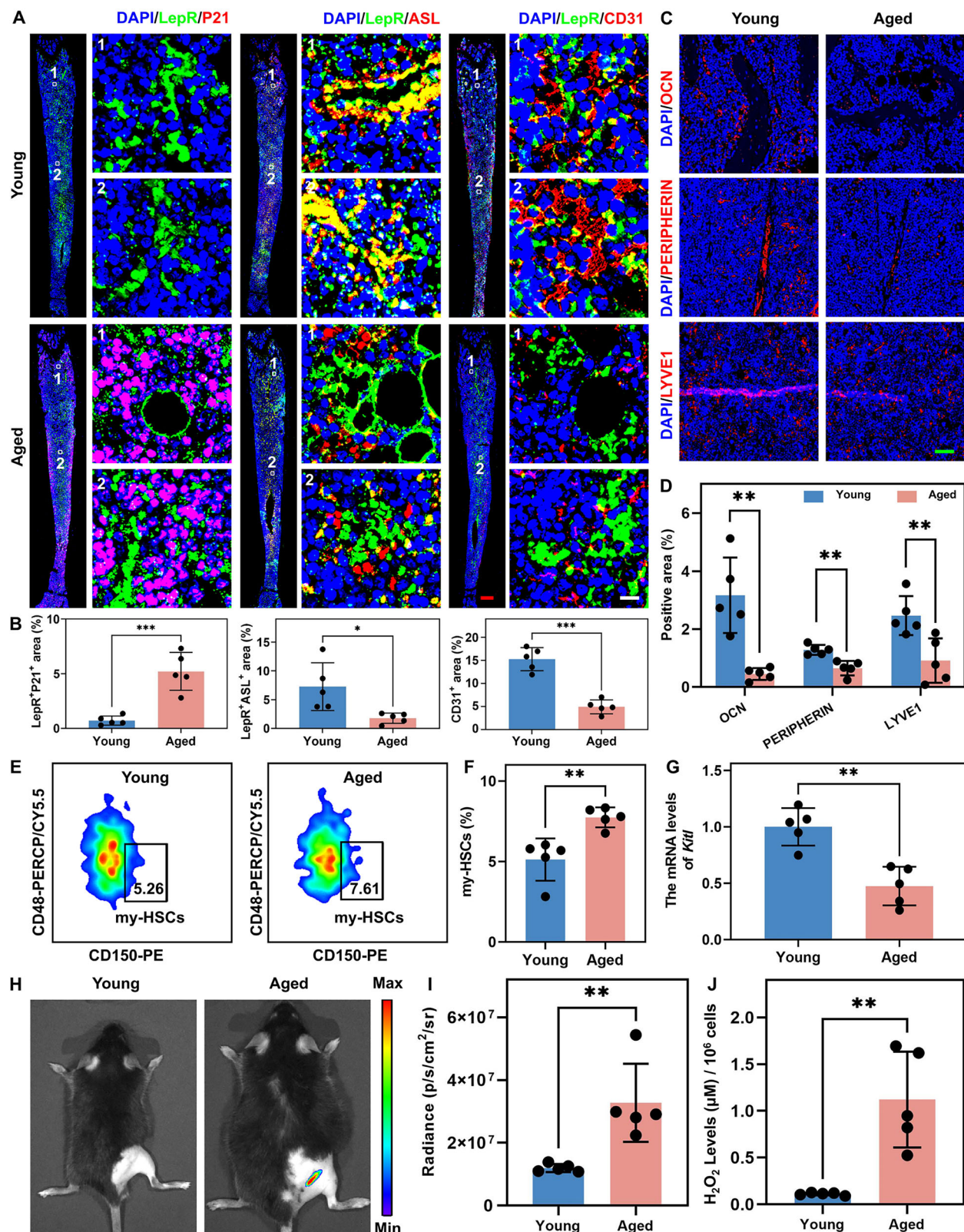


**Fig. 2 | Decreased ASL, increased senescence and H<sub>2</sub>O<sub>2</sub> in the LepR<sup>+</sup> cells of aged mice. A–D** Levels of P21, ASL, CD31, OCN, PERIPHERIN and LYVE1 in young or aged mice and quantitative results ( $n = 5$  mice). Scale bars, 500  $\mu$ m (red), 10  $\mu$ m (white) and 50  $\mu$ m (green). **E, F** Proportion of my-HSCs (Lineage<sup>+</sup>Sca-1<sup>+</sup>c-Kit<sup>+</sup> (LSK) CD48<sup>+</sup>CD150<sup>high</sup> HSCs) in the femoral BM of young or aged mice ( $n = 5$  mice). **G** Quantification of the mRNA levels of SCF (encoded by *Kitl* gene) in sorted LepR<sup>+</sup>

cell ( $n = 5$  mice). **H, I** The fluorescence intensity of H<sub>2</sub>O<sub>2</sub> probe in the femoral BM of young and aged mice. **J** H<sub>2</sub>O<sub>2</sub> content in the femoral BM of young or aged mice ( $n = 5$  mice). The data are shown as the means  $\pm$  SDs. Statistical significance was determined by two-tailed unpaired Student's *t* test (two groups); \* $P$  < 0.05, \*\* $P$  < 0.01, \*\*\* $P$  < 0.005. Source data are provided as a Source Data file.

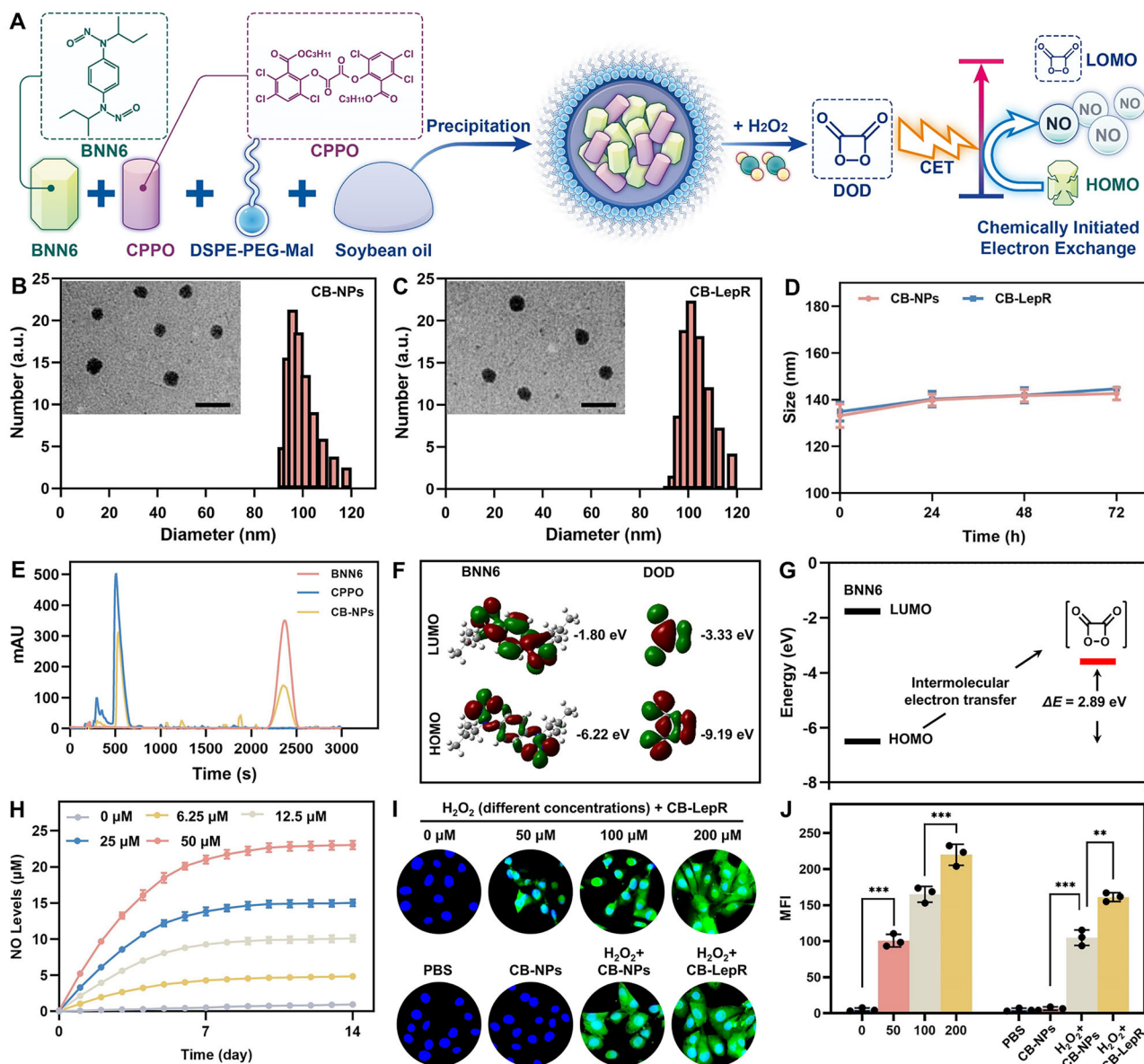


**Fig. 3 | Design of CB-NPs and CB-LepR for NO production.** **A** Preparation of CB-NPs. **B, C** Transmission electron micrographs (TEM) and diameter distributions measured by dynamic light scattering (DLS) of CB-NPs and CB-LepR, respectively. Scale bar, 200 nm. **D** Size stability of CB-NPs and CB-LepR detected by DLS ( $n = 3$  independent experiments). **E** HPLC chromatograms of CPPO, BNN6, and CB-NPs. **F, G** Energy levels of BNN6 and the active DOD. **H** Levels of NO released after co-incubation of  $H_2O_2$  (different concentrations) with CB-LepR. ( $n = 3$  independent

experiments). **I, J** Fluorescence images of LepR<sup>+</sup> cells stained with an NO fluorescent probe (DAF-FM DA) after different treatments ( $n = 3$  independent experiments). The data are shown as the means  $\pm$  SDs. Statistical significance was determined by two-tailed unpaired Student's *t* test (two groups) or one-way ANOVA with Dunnett's multiple comparison tests (multiple groups); \*\* $P < 0.01$ , \*\*\* $P < 0.005$ . Source data are provided as a Source Data file.

72 h incubation of BM-derived LepR<sup>+</sup> cells at 200  $\mu M$  (Supplementary Fig. 5A), the LepR<sup>+</sup> cells were incubated with  $H_2O_2$  (200  $\mu M$ ) and CB-LepR (0, 50, 100, 150, or 200  $\mu g/mL$ ) for 72 h. No significant cell death was observed in the group containing 50  $\mu g/mL$  CB-LepR compared with the other groups; hence, this concentration was chosen for further tests (Supplementary Fig. 5B, C). Since the release of NO is a prerequisite for intervention in senescent cells, the intracellular NO release behavior of CB-LepR was assessed by an NO probe (4-amino-5-methylamino-2',7'-difluorescein diacetate, DAF-FM DA), which can be rapidly deacetylated by intracellular esterases to form DAF-FM upon entry into living cells and then react with NO to produce green fluorescence<sup>29,30</sup>. The results revealed strong green fluorescence in the cells treated with CB-LepR when exposed to  $H_2O_2$ , the intensity of which was positively correlated with the concentration of  $H_2O_2$

(Fig. 3I, J), indicating that  $H_2O_2$  is essential for the release of NO from the NO nanopumps. Notably, the green fluorescence in CB-LepR-treated cells was brighter than that in CB-NPs treated cells, possibly due to the LepR-mediated targeting effect with improved cellular uptake of nanoparticles.

### LepR-targeting efficiency of the nanopumps in vivo

To investigate the targeting efficiency of CB-LepR against LepR<sup>+</sup> cells in vivo, CB-NPs or CB-LepR were conjugated with CY5.5 to form CB<sup>CY5.5</sup>-NPs or CB<sup>CY5.5</sup>-LepR. The aged mice femurs were collected at 7 days after local injection of CB<sup>CY5.5</sup>-NPs or CB<sup>CY5.5</sup>-LepR. The LepR-targeting efficiency of NO nanopumps was observed by the fluorescence co-localization of CY5.5 from NO nanopumps and FITC-conjugated antibody-labeled LepR<sup>+</sup> cells. CB<sup>CY5.5</sup>-NPs situated in the central BM of aged



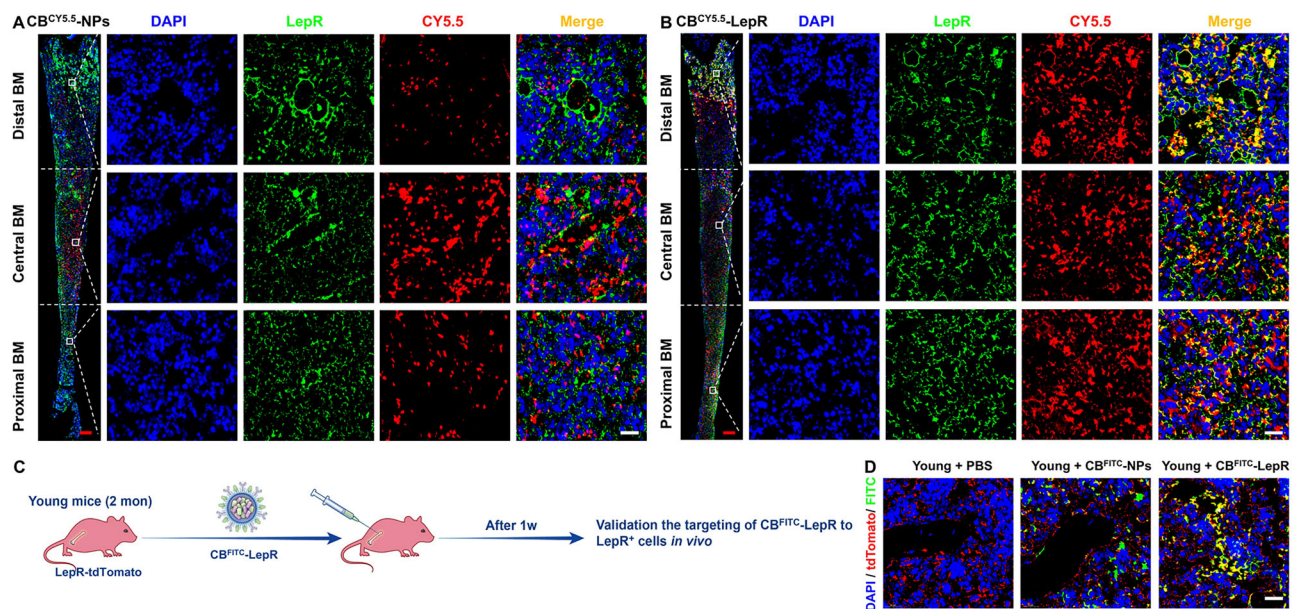


**Fig. 4 | Assessment of LepR<sup>+</sup> cells-targeting properties.** **A, B** Fluorescence imaging of the ability of CB<sup>CYS.5</sup>-NPs and CB<sup>CYS.5</sup>-LepR to target LepR<sup>+</sup> cells after FITC-conjugated secondary antibody labeling of LepR<sup>+</sup> cells in femoral sections from the

aged mice. Scale bars, 500  $\mu$ m (red) and 50  $\mu$ m (white). **C, D** Schematic diagram and representative fluorescence images of CB<sup>FITC</sup>-LepR-targeted LepR<sup>+</sup> cells in LepR-tdTomato mice. Scale bar, 50  $\mu$ m.

mice exhibited minimal colocalization with LepR<sup>+</sup> cells. However, CB<sup>CYS.5</sup>-LepR exhibited superior LepR<sup>+</sup> cell-targeting ability in the whole BM compared with non-targeted CB<sup>CYS.5</sup>-NPs (Fig. 4A, B). Moreover, cells from the BM cavity were collected at 7 days after local injection of CB<sup>CYS.5</sup>-NPs and CB<sup>CYS.5</sup>-LepR for flow cytometric analysis. A total of  $52.8 \pm 12.2$  % of the LepR<sup>+</sup> cells were specifically bound by CB<sup>CYS.5</sup>-LepR after 7 days of injection as compared to  $6.2 \pm 2.7$  % in the CB<sup>CYS.5</sup>-NPs group. However, the cellular uptake of CB<sup>CYS.5</sup>-NPs and CB<sup>CYS.5</sup>-LepR in LepR<sup>+</sup> cells was low, indicating the targeting effect of CB-LepR toward LepR<sup>+</sup> cells (Supplementary Fig. 6A, B).

Next, LepR-tdTomato mice, in which LepR cells can be traced, were applied to track the targeting efficiency of CB-LepR to LepR<sup>+</sup> cells in vivo (Fig. 4C, D). Femurs were collected 7 days after young + PBS, young + CB<sup>FITC</sup>-NPs, or young + CB<sup>FITC</sup>-LepR treatment. As shown in Fig. 4D, the young + CB<sup>FITC</sup>-LepR group presented more pronounced co-localization of tdTomato and FITC in the femoral marrow cavity when compared to the other groups, demonstrating that LepR antibody-conjugated nanopumps enable specific targeting of the LepR<sup>+</sup> cells in the BM for precise and quantitative intracellular release of NO. Since studies have confirmed that a high fraction of systemically administered leptin is retained in the BM, suggesting that leptin receptors are abundantly localized in the BM<sup>31</sup>. Then, we injected CB-LepR by the tail vein approach to evaluate the systemic BM targeting property. The results showed a gradual increase in fluorescence intensity over time in the bones of the mice injected with CB<sup>CYS.5</sup>-LepR for 12 h (Supplementary Fig. 6C, D), especially in the spine, thorax, and femur, indicating that the modification of the LepR antibody endows the NO nanopump with superior systemic BM targeting ability. Although a gradual decrease in fluorescence intensity was subsequently observed in the mouse skeleton at 12 h after injection, the fluorescent signal was still obvious in the mouse skeleton at 24 h after injection (Supplementary Fig. 6C, D). Notably, no significant organ damage and immunotoxicity was observed after systemic treatment with CB-LepR, indicating that CB-LepR possesses a favorable biosafety profile (Supplementary Fig. 6J, K).

#### H<sub>2</sub>O<sub>2</sub> scavenging and NO generation by CB-LepR

Inspired by the targeting effect of CB-LepR against LepR<sup>+</sup> cells in the BM, the capacity of CB-LepR to scavenge H<sub>2</sub>O<sub>2</sub> and produce NO was

assessed after it entered the BM cavity (Fig. 5A). In vivo, fluorescence imaging revealed significant H<sub>2</sub>O<sub>2</sub> accumulation in the BM cavity of aged mice, which was eliminated following the administration of CB-LepR (Fig. 5B, C). When the whole content from the BM was flushed, the intracellular H<sub>2</sub>O<sub>2</sub> concentration of the aged BM effectively decreased from 7.9  $\mu$ M to 0.6  $\mu$ M after CB-LepR treatment (Fig. 5D). Notably, the H<sub>2</sub>O<sub>2</sub> concentration was markedly reduced solely in LepR<sup>+</sup> cells but remained unchanged in LepR<sup>-</sup> cells (Fig. 5E). Additionally, the NO concentration in the LepR<sup>+</sup> cells remained at 4  $\mu$ M for 1 week (Fig. 5F), indicating that the targeted H<sub>2</sub>O<sub>2</sub> scavenging and specific NO release by CB-LepR in the LepR<sup>+</sup> cells of the aged BM could potentially exerting a profound influence on rejuvenating senescent the LepR<sup>+</sup> cells and further facilitate the reconstruction of the aged BM. To further demonstrate the NO release behavior of CB-LepR in LepR<sup>+</sup> cells, we dynamically observed the NO release process within LepR<sup>+</sup> cells after uptake of CB<sup>CYS.5</sup>-LepR via live-cell imaging microscopy (Fig. 5G). No green fluorescence was observed in the cells incubated with PBS (Supplementary Fig. 7), whereas the cells incubated with H<sub>2</sub>O<sub>2</sub> presented progressively stronger green fluorescence (Fig. 5H). These findings support the theory that CB-LepR releases NO only after being exposed to H<sub>2</sub>O<sub>2</sub> via the chemical excitation of BNN6.

#### NO nanopumps rejuvenate senescent LepR<sup>+</sup> cells and improve their osteogenic differentiation capacity in vitro

LepR<sup>+</sup> cells in the BM are known to be a major source of bone and adipocytes in the adult BM<sup>2,32</sup>. Since the direction of senescent LepR<sup>+</sup> cell differentiation strongly influences the development of bone senescence, we explored the role of CB-NPs and CB-LepR in LepR<sup>+</sup> cell senescence and osteogenic or adipogenic differentiation (Fig. 6A). The NO nanopumps were found to exhibit superior anti-senescence ability via senescence-associated  $\beta$ -galactosidase (SA- $\beta$ -Gal) staining (Fig. 6B, C). Compared with those in the other groups, alkaline phosphatase (ALP) and alizarin red (ARS) staining revealed increased osteogenesis and more mineralized nodules in the LepR<sup>+</sup> cells treated with CB-NPs or CB-LepR in osteogenic induction medium containing H<sub>2</sub>O<sub>2</sub> (100  $\mu$ M) (Fig. 6D–G). Enhanced adipogenic differentiation and lipid droplet formation was observed via Oil Red O (ORO) staining in LepR<sup>+</sup> cells treated with adipogenic induction medium supplemented with H<sub>2</sub>O<sub>2</sub> (100  $\mu$ M), whereas these effects were significantly reduced

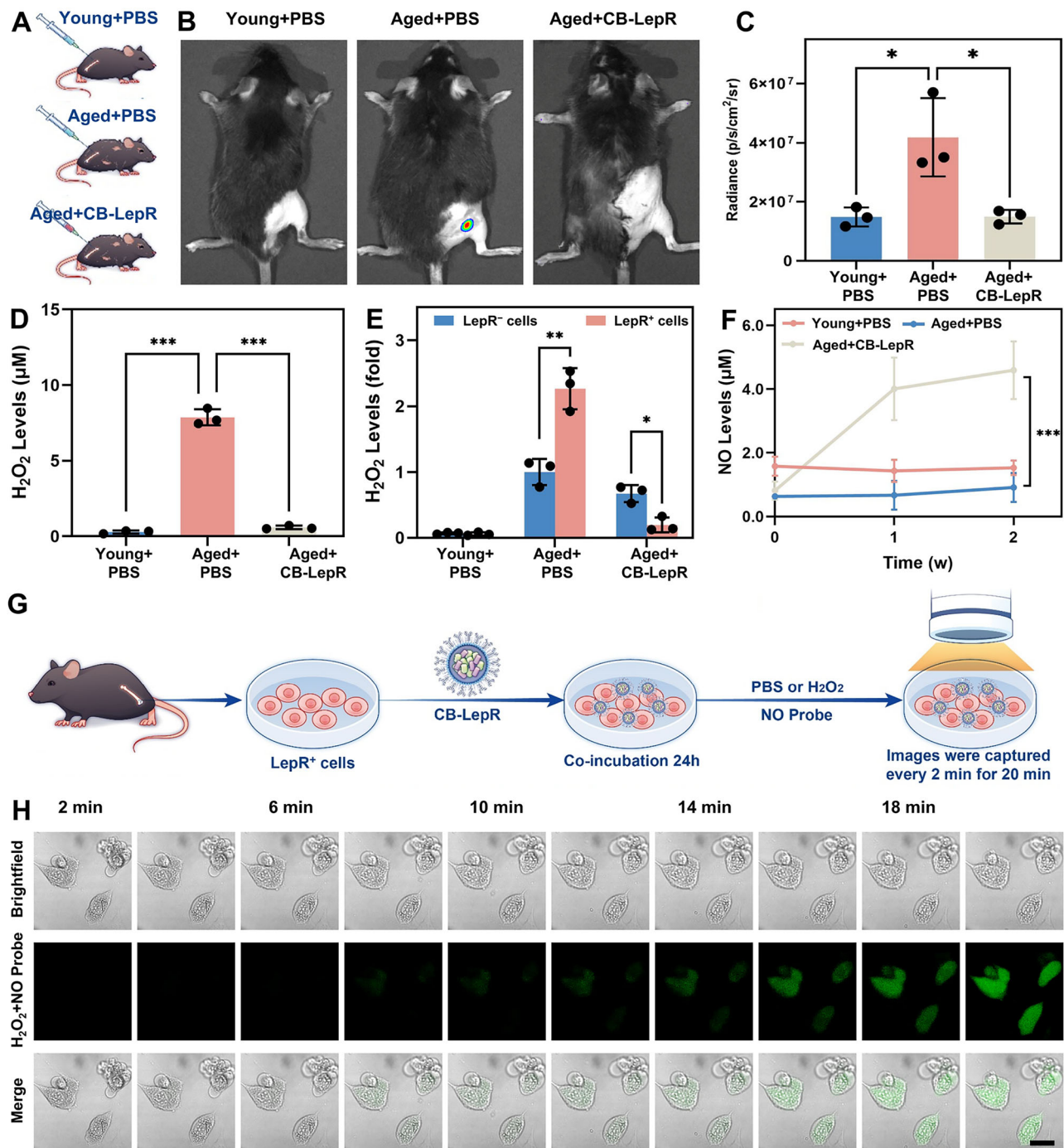


**Fig. 5 | NO nanopumps effectively remove H<sub>2</sub>O<sub>2</sub> and generate NO. A** Schematic diagram of the detection of H<sub>2</sub>O<sub>2</sub> and NO in mice subjected to different treatments. **B, C** Representative fluorescence images and quantitative analysis of H<sub>2</sub>O<sub>2</sub> probed-treated different mice ( $n = 3$  mice). **D** Intracellular levels of H<sub>2</sub>O<sub>2</sub> in the BM of the different groups after 2 weeks ( $n = 3$  mice). **E** Intracellular H<sub>2</sub>O<sub>2</sub> levels in sorted LepR<sup>+</sup> and LepR<sup>-</sup> cells from different treated mice ( $n = 3$  mice). **F** Intracellular NO levels in sorted LepR<sup>+</sup> cells from different treated mice ( $n = 3$  mice). **G** Schematic

diagram of a live-cell workstation capturing NO release from CB-LepR.

**H** Representative images of NO release from LepR<sup>+</sup> cells after co-incubation with CB-LepR + H<sub>2</sub>O<sub>2</sub>. 3 times each experiment was repeated independently with similar results. Scale bar, 50 μm. The data are shown as the means ± SDs. Statistical significance was determined by two-tailed unpaired Student's *t* test (two groups) or one-way ANOVA with Dunnett's multiple comparison tests (multiple groups); \* $P < 0.05$ , \*\* $P < 0.01$ , \*\*\* $P < 0.005$ . Source data are provided as a Source Data file.

in the H<sub>2</sub>O<sub>2</sub> + CB-NPs and H<sub>2</sub>O<sub>2</sub> + CB-LepR groups (Fig. 6H, I). We further evaluated the expression of the *Alp*, osteocalcin (*Ocn*), osterix (*Osx*), runt-related transcription factor 2 (*Runx2*) genes (osteogenesis-related genes), fatty acid binding protein 4 (*Fabp4*), and peroxisome proliferator-activated receptor  $\gamma$  (*Ppar\gamma*) genes (adipogenesis-related genes) in each group to confirm our observations. Consistent with the staining data, H<sub>2</sub>O<sub>2</sub> resulted in increased expression of adipogenesis-

related genes and decreased expression of osteogenesis-related genes in the LepR<sup>+</sup> cells (Fig. 6J–O). However, the adipogenic differentiation of LepR<sup>+</sup> cells caused by H<sub>2</sub>O<sub>2</sub> was significantly reversed after intervention with CB-NPs and CB-LepR. Furthermore, the H<sub>2</sub>O<sub>2</sub> + CB-LepR treatment resulted in the most significant osteogenic differentiation among all the groups, which could benefit from the LepR<sup>+</sup> cell-targeting effect. Collectively, the results confirmed that CB-LepR could



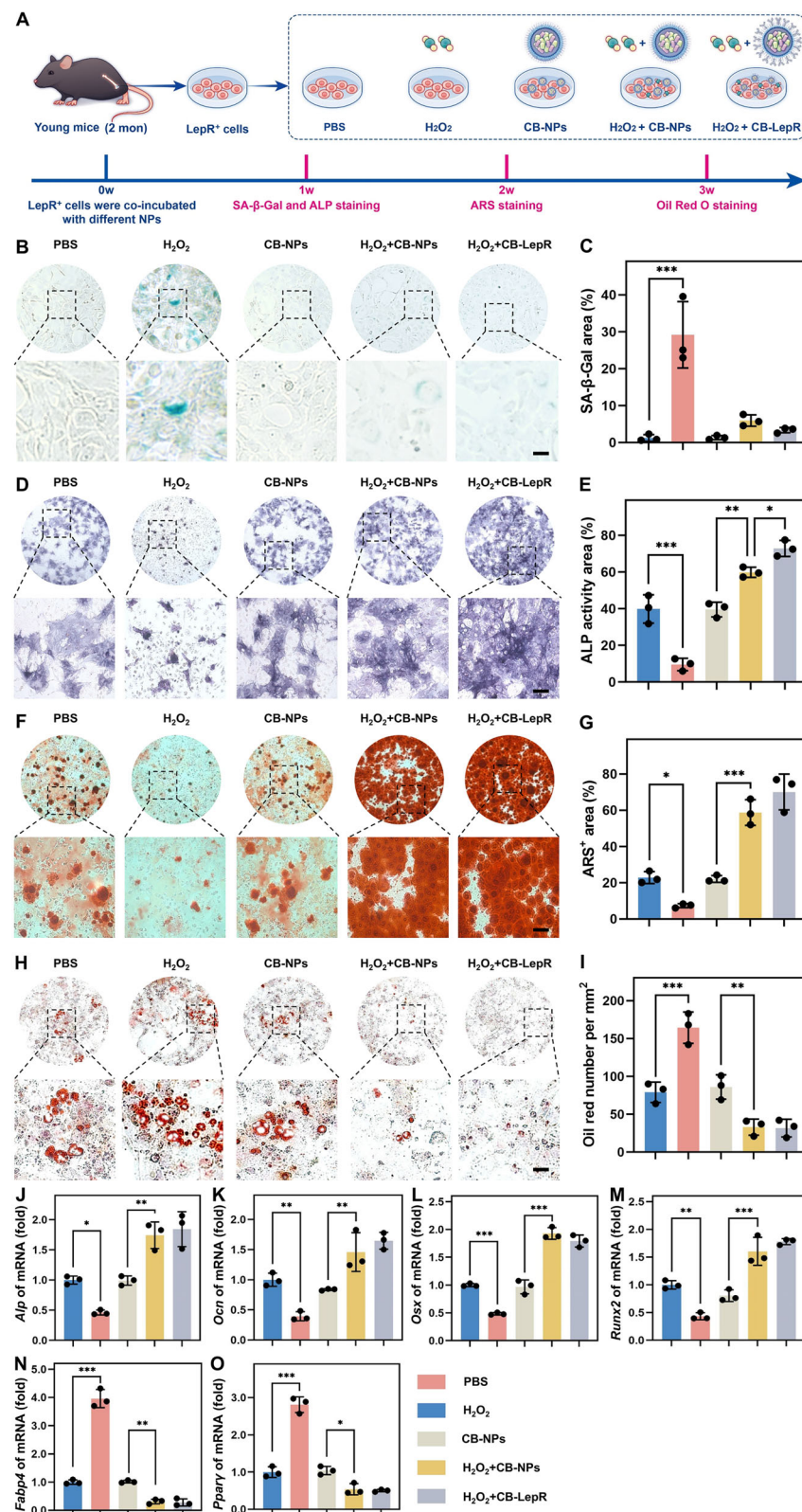


**Fig. 6 | NO nanopumps alleviate the senescence of LepR<sup>+</sup> cells and reverse their differentiation fate.** **A** In vitro treatment schedule. **B, C** Representative images and quantitative analysis of SA-β-Gal staining in different treatment groups ( $n = 3$  independent experiments). Scale bar, 100 μm. **(D–G)** Representative images and quantitative analysis of ALP and ARS staining in different treatment groups ( $n = 3$  independent experiments). Scale bar, 100 μm. **H, I** Representative images and quantitative analysis of Oil red O staining in different treatment groups ( $n = 3$

independent experiments). Scale bar, 100 μm. **J–O** qPCR analysis of osteogenic (*Alp*, *Ocn*, *Osx*) and adipogenic (*Fabp4* and *Pparγ*) gene expression in LepR<sup>+</sup> stromal cells ( $n = 3$  independent experiments). The data are shown as the means ± SDs. Statistical significance was determined by one-way ANOVA with Dunnett's multiple comparison tests (multiple groups); \* $P < 0.05$ , \*\* $P < 0.01$ , \*\*\* $P < 0.005$ . Source data are provided as a Source Data file.



rejuvenate LepR<sup>+</sup> cells from senescence and promote their osteogenic differentiation instead of adipogenic differentiation after exposure to H<sub>2</sub>O<sub>2</sub>.

### Local NO release reestablishes the homeostasis of aging-induced BM collapse

Inspired by the rejuvenation effect of CB-LepR on LepR<sup>+</sup> cells under senescent conditions, the ability of CB-LepR to prevent aging-induced BM collapse in vivo was further assessed via local injection into the femurs of aged mice (Fig. 7A). Micro-computed tomography (microCT) analysis revealed a significant increase in the trabecular bone volume and a decrease in the trabecular space in the femurs of the aged + CB-NPs and aged + CB-LepR groups compared with those of the aged control group (Fig. 7B–F). A phenomenon consistent with locally BM injection was observed in the femurs of mice that received systemic treatment (Supplementary Fig. 6E–I). These alterations were suspected to be caused by the release of NO from CB-NPs and CB-LepR in the milieu of bone senescence to stimulate bone growth upon exposure to H<sub>2</sub>O<sub>2</sub>. Compared with the CB-LepR group, the CB-NPs group exhibited inferior bone salvage, which may be related to the fact that CB-NPs only reduced H<sub>2</sub>O<sub>2</sub> in the aged BM microenvironment. The superior targeting of LepR<sup>+</sup> cells by CB-LepR resulted in less bone loss in the aged + CB-LepR group than in the other groups. Furthermore, we observed a significant decrease in the number of senescent LepR<sup>+</sup> cells, adipocytes, osteoclasts and a notable increase in osteogenesis in the BM of the aged + CB-LepR groups compared with the aged + PBS group (Fig. 7G, H), which was attributed to the targeted H<sub>2</sub>O<sub>2</sub> consumption and NO generation of CB-LepR in LepR<sup>+</sup> cells.

LepR<sup>+</sup> cells in the BM effectively drive vascular, lymphatic and nerve fiber regeneration<sup>4–7</sup>. Thus, the ability of CB-LepR to prevent BM collapse was further investigated. Through immunofluorescence staining, a reduction in vascular, nerve and lymphatic vessels was observed in femoral sections from aged mice, whereas these changes were significantly reversed in femurs from aged + CB-LepR mice (Fig. 7I). Moreover, compared with the increased number of my-HSCs in the aged group, the proportion of my-HSCs in the BM of the aged + CB-LepR group was significantly decreased (Fig. 7J, K). We further analyzed the RNA-seq dataset from the sorted LepR<sup>+</sup> cells and found changes in SCf (encoded by *Kitl* gene), *Vegf-c* and *Ngf*. The gene expression levels of *Kitl*, *Vegf-c* and *Ngf* were significantly reduced in the LepR<sup>+</sup> cells from the aged + PBS group than in those from the young + PBS group, while increased in the LepR<sup>+</sup> cells from the CB-LepR treated aged mice (Fig. 7L), which provides additional support for demonstration of the BM restoration. These phenomena were largely due to the precise reversal of LepR<sup>+</sup> cell senescence in the BM microenvironment by CB-LepR. The metabolism of NO nanopumps in vivo is critical for their application. Following a 1-week local injection of CB-LepR, a substantial number of fluorescent signals were observed in the liver and kidney, indicating that NO nanopumps are metabolized predominantly in these organs. The fluorescence signals of the NO nanopumps diminished over time, and the NO nanopumps were gradually degraded by the liver and kidney within 4 weeks without significant toxicity (Supplementary Fig. 8A, B).

### CB-LepR released NO activates glycolysis in LepR<sup>+</sup> cells to rescue senescence

To further investigate the mechanism by which the NO nanopump affects the senescence of LepR<sup>+</sup> cells, RNA sequencing (RNA-seq) was performed. Kyoto Encyclopedia of Genes and Genomes (KEGG) pathway analysis and gene set enrichment analysis (GSEA) of the in vitro sequencing data revealed that the glycolysis signaling pathway was down-regulated in the H<sub>2</sub>O<sub>2</sub> group, which was accompanied by the upregulation of the cellular senescence signaling pathway (Supplementary Fig. 9A, B). Conversely, the KEGG pathway analysis of the CB-LepR group compared with the H<sub>2</sub>O<sub>2</sub> group revealed enrichment of

terms related to glycolysis (Fig. 8A). Moreover, GSEA demonstrated that CB-LepR reversed cellular senescence by triggering glycolysis (Fig. 8B). Additionally, Venn analysis revealed 20 glycolysis-related genes whose expression differed significantly between the H<sub>2</sub>O<sub>2</sub> and PBS groups (Fig. 8C). These differences were significantly reversed after CB-LepR intervention (Fig. 8D). To further validate the effect of CB-LepR on LepR<sup>+</sup> cell senescence, we sorted LepR<sup>+</sup> cells from the femoral BM of young, aged, and aged + CB-LepR mice for in vivo LepR<sup>+</sup> cells RNA sequencing. GSEA of the in vivo sequencing data revealed significant downregulation of cellular senescence signals in the aged + CB-LepR group compared with the aged + PBS group (Supplementary Fig. 9C). Notably, among the 16 glycolysis-related genes that were differentially expressed between age + PBS and young + PBS groups, 10 DEGs were reversed in the aged + CB-LepR group (Supplementary Fig. 9D). The RNA-seq data provide evidence that NO nanopumps reverse LepR<sup>+</sup> cells senescence by activating the glycolysis signaling pathway.

The SA-β-Gal staining results further supported this hypothesis. The senescence of the LepR<sup>+</sup> cells in the H<sub>2</sub>O<sub>2</sub> group was markedly diminished after treatment with CB-LepR, and cellular senescence reappeared after the addition of 2-deoxyglucose (2-DG, a glycolysis inhibitor) to the H<sub>2</sub>O<sub>2</sub> + CB-LepR group (Fig. 8E, F). To substantiate the relationship between NO release and glycolytic activation, we inhibited glycolysis via 2-DG and obstructed NO synthesis with NG-nitro-L-arginine methyl ester (L-NAME) in vivo, and subsequently evaluated their effects on senescence in LepR<sup>+</sup> cells treated with CB-LepR through LepR/P21 fluorescence staining. The results demonstrated that CB-LepR significantly decreased the P21 expression in the LepR<sup>+</sup> cells in the aged mice. However, P21 expression was significantly increased in the LepR<sup>+</sup> cells in the aged + CB-LepR with 2-DG and L-NAME injection (Supplementary Fig. 10A, B), suggesting that the anti-aging effects of the released NO could be due to the glycolytic pathway activation. The SA-β-Gal staining data and P21 immunofluorescence staining were consistent with the RNA-seq data, indicating the importance of the glycolysis signaling pathway in CB-LepR-mediated regulation of LepR<sup>+</sup> cell aging. According to the qPCR results, pyruvate kinase isozyme M2 (*Pkm2*, a key gene in glycolysis) and lactate dehydrogenase A (*Ldha*, a key gene in glycolysis) expression levels in cellular nucleic acid extracts decreased after exposure to H<sub>2</sub>O<sub>2</sub> but increased after exposure to CB-LepR (Fig. 8G). Using a Seahorse XFe96 analyzer, we calculated the extracellular acidification rate (ECAR), which quantifies glycolysis, in each group. The baseline and maximal glycolytic capacities of the LepR<sup>+</sup> cells were reduced by the addition of H<sub>2</sub>O<sub>2</sub> but were partially restored following CB-LepR treatment (Fig. 8H–J). These results suggest that NO-mediated cellular senescence is based on the regulation of glycolysis.

## Discussion

The BM maintains homeostasis through a variety of cells working in concert<sup>33</sup>. The cells in the BM inevitably undergo senescence with aging. Recent studies have shown that senescent osteoblasts exhibit reduced bone formation capacity, which promotes the development of damaged BM homeostasis<sup>34</sup>. BM adipocytes have also been found to contribute to the accumulation of senescent cells and abnormalities in the bone microenvironment through the SASP<sup>35</sup>. Senescent immune cells, another population in the BM with common features, including decreased immune function and increased release of inflammatory factors, are manifested mainly by a decreased immune response of the organism to endogenous and exogenous antigens, leading to a decreased ability to clear senescent cells and a vicious cycle of inflammation–senescence<sup>36</sup>. A subpopulation of pro-inflammatory and pro-senescent immune cells consisting of grancalcin (GCA)-positive macrophages and neutrophils in senescent BM has been reported to secrete GCA to promote bone aging<sup>37</sup>. Furthermore, the initiation of secondary senescence responses by senescent immune cells has been

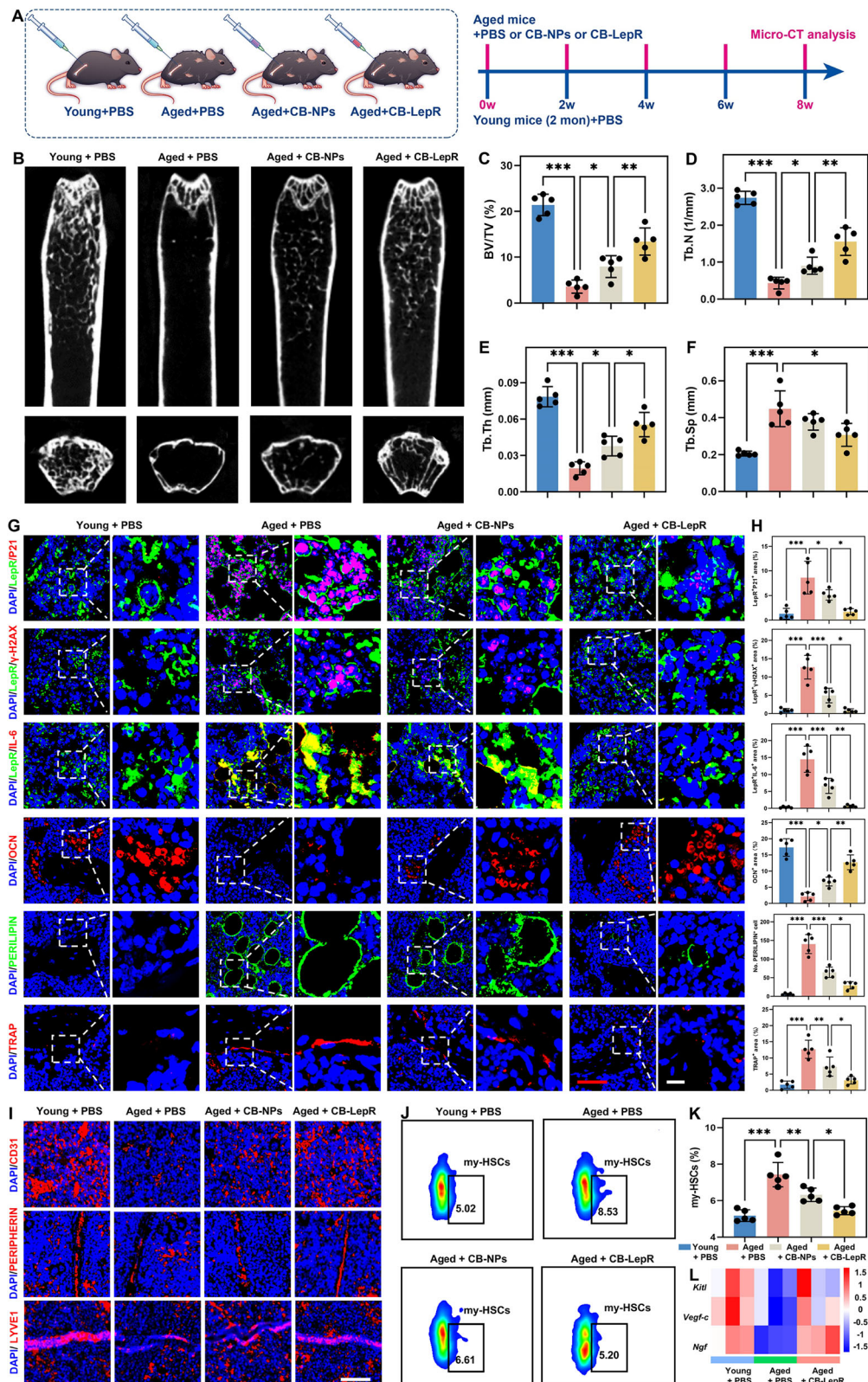


**Fig. 7 | CB-LepR exhibits anti-BM microenvironment aging efficacy.**

**A** Treatment schedule in vivo. **B–F** Representative micro-CT images and quantitative analysis of the bone volume per tissue volume (BV/TV), trabecular bone number (Tb.N), trabecular thickness (Tb.Th), and trabecular separation (Tb.Sp) ( $n = 5$  mice). **G–H** Immunofluorescence staining for senescence, bone formation, lipid droplet formation and osteoclastic activity ( $n = 5$  mice). Scale bars, 50 μm (red) and 10 μm (white). **I** Representative fluorescence images of LepR<sup>+</sup> cells

promoting lymphatic, vascular, and neural regeneration. Scale bar, 50 μm.

**J, K** Proportion of my-HSCs in different treatment groups ( $n = 5$  mice). **L** Heatmap of SCF (encoded by *Kitl* gene), *Vegf-c* and *Ngf* in the young + PBS, aged + PBS, and aged + CB-LepR groups. The data are shown as the means ± SDs. Statistical significance was determined by one-way ANOVA with Dunnett's multiple comparison tests (multiple groups); \* $P < 0.05$ , \*\* $P < 0.01$ , \*\*\* $P < 0.005$ . Source data are provided as a Source Data file.



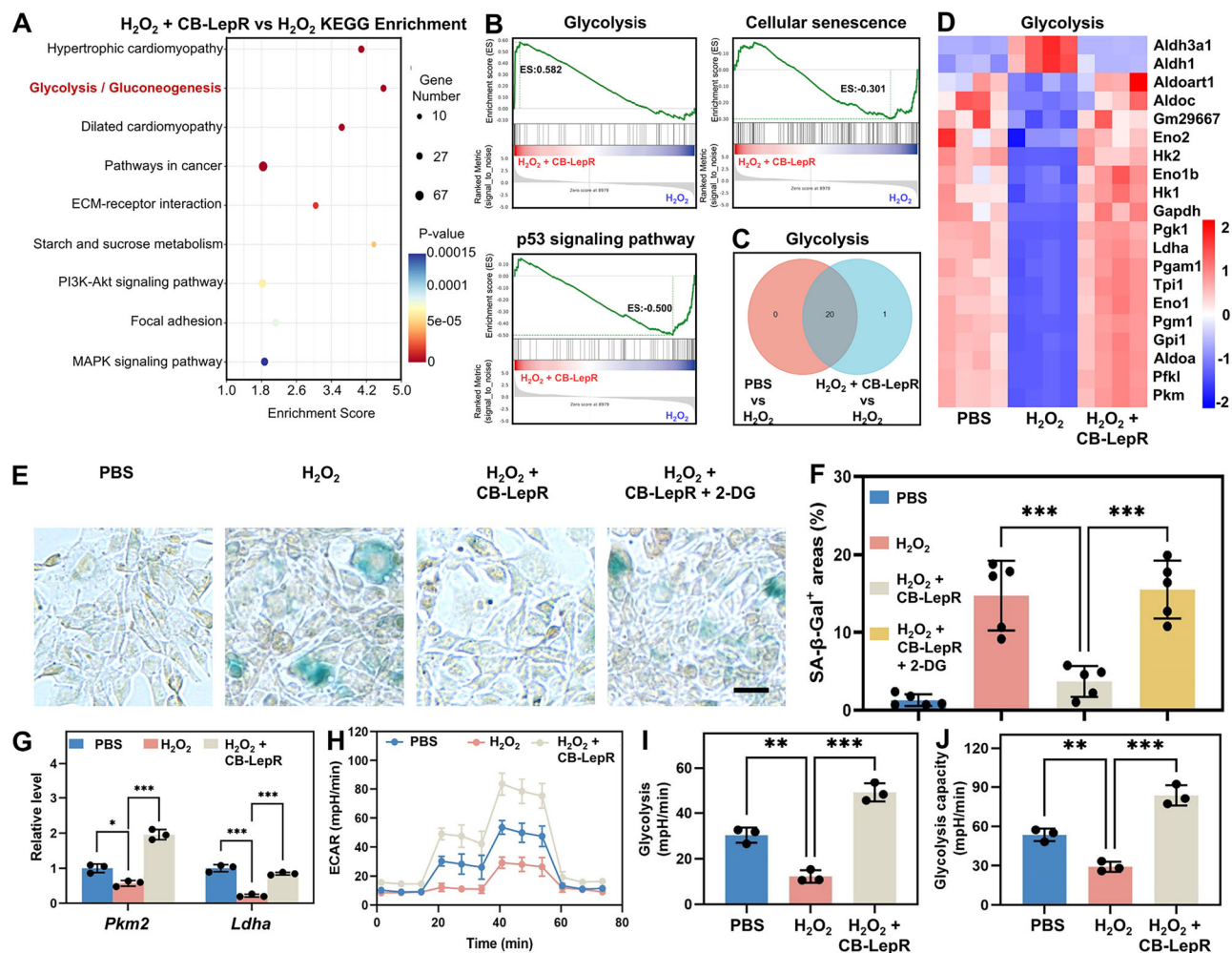


**Fig. 8 | NO nanopumps upregulate the glycolytic pathway to alleviate LepR<sup>+</sup> cell senescence.** **A** KEGG pathway analysis of the  $H_2O_2$  + CB-LepR and  $H_2O_2$  groups. **B** GSEA of the  $H_2O_2$  + CB-LepR and  $H_2O_2$  groups. **C** Venn analyses of genes related to glycolysis in the PBS,  $H_2O_2$ , and  $H_2O_2$  + CB-LepR groups. **D** Heatmap of differentially expressed glycolysis-related genes in the PBS,  $H_2O_2$  and  $H_2O_2$  + CB-LepR groups. **E, F** Representative images and quantitative analysis of SA-β-Gal staining ( $n = 3$  independent experiments). Scale bars, 50 μm. **G** mRNA levels of genes in the

glycolytic pathway, including *Pkm2* and *Ldha* ( $n = 3$  independent experiments).

**H–J** Seahorse assay of glycolytic activity (ECAR) in LepR<sup>+</sup> cells after 24 h of different treatments ( $n = 3$  independent experiments). The data are shown as the means ± SDs. Statistical significance was determined by one-way ANOVA with Dunnett's multiple comparison tests (multiple groups); \* $P < 0.05$ , \*\* $P < 0.01$ , \*\*\* $P < 0.005$ . Source data are provided as a Source Data file.

demonstrated to cause widespread dissemination of senescence in organisms<sup>38</sup>. Studies have revealed that senescent BM monocytes/macrophages propagate senescence through extracellular vesicles to multiple tissues, including bone tissue and the liver<sup>39</sup>. T cells, a pivotal element of adaptive immunity, undergo a transition to a pro-inflammatory state within senescent BM, resulting in a chronic inflammatory infiltrate<sup>40</sup>. Furthermore, an increased number of senescent B cells, which secrete high levels of TNF-α, have been observed in the BM of aged mice. TNF-α has been demonstrated to impede the production of healthy B cells, consequently resulting in a decrease in the number and function of B cell precursors within senescent BM<sup>41</sup>. Consequently, these alterations collectively diminish the immune system's capacity to combat infection and promote BM senescence. Senescent LepR<sup>+</sup> cells are key drivers responsible for damaged BM homeostasis under aged conditions. LepR<sup>+</sup> cells persist throughout the life cycle of bone and regulate regeneration of the BM by secreting a variety of growth factors<sup>3–6</sup>. Senescent LepR<sup>+</sup> cells show reduced secretory and impaired regenerative capacity; thus, these cells could be potential therapeutic targets for the prevention and management of disrupted BM homeostasis during aging. Attempts at

gene editing, small-molecule therapy, and gut microbiota have partially reversed the senescence of LepR<sup>+</sup> cells<sup>42–45</sup>, but the high degree of off-target effects, low degree of tissue targeting, and poor stability limit their anti-aging capabilities. Here, we constructed a NO nanopump that specifically targets LepR<sup>+</sup> cells and rejuvenates senescent LepR<sup>+</sup> cells via in situ chemiexcitation of NO donors to release NO in the LepR<sup>+</sup> cells of the osteoporotic microenvironment.

NO-based therapies have emerged as potential treatments for diseases within the skeletal system<sup>46</sup>. To supply NO gas in vivo, various nanocarriers have been designed for NO donor encapsulation by utilizing the specific properties of nanoparticles, including packaging stability, biocompatibility, tissue targeting, etc. Since the convenient and sustained release of NO in bone tissue is a challenge for the development of NO nanomaterials and their anti-BM aging application<sup>22</sup>, we attempted to fabricate an in situ NO release system (CB-NPs) based on BNN6, CPPO, soybean oil and the amphiphilic polymer DSPE-PEG-MAL through a co-precipitation method. Compared with the conventional NO delivery system, the constructed CB-LepR offers the following advantages: (1) The complexity of conversion and cascade is avoided, and NO is quantitatively released in situ in aged

BM with a high level of  $\text{H}_2\text{O}_2$  by direct chemical excitation. (2) The addition of soybean oil as a retardant to the construct significantly extends the half-life of NO. (3) NO produced by extracellular NO nanopumps partially regulates the aged BM microenvironment at an early stage. (4) Modification with the LepR antibody promotes the targeted delivery of NO nanopumps and controlled production of NO in LepR<sup>+</sup> cells, thereby significantly rescuing cellular senescence.

The activities of humans or tissues require the involvement of energy metabolism. Compared with young individuals, aged individuals always exhibit reduced energy metabolism<sup>47</sup>. Current research suggests that the dysregulation of energy metabolism is strongly involved in the aging process<sup>48</sup>. Senescent cells experience disruptions in their energy metabolism, and their mitochondrial oxygen consumption rate increases, which leads to an increase in the formation of free radicals and accelerates aging by increasing oxidative damage to body tissues<sup>47,48</sup>. Increasing evidence suggests that a lack of NO affects glycolysis in the cellular energy metabolism process<sup>49–51</sup>, leading to cellular senescence. Therefore, NO supplementation may rescue cellular senescence by regulating energy metabolism. NO may activate glycolysis through multiple pathways. NO has been shown to restore glycolysis by upregulating the expression of Slc2a1 and glucose transporter protein 4<sup>52–54</sup>. In addition, data support the involvement of the soluble guanylyl cyclase/cyclic guanosine monophosphate pathway in glucose uptake in skeletal muscle cells<sup>55</sup>. Thus, regulating energy metabolism through NO supplementation to rescue cellular senescence may be an effective strategy to reverse damage to the BM microenvironment. Our results showed that NO could reverse senescence in LepR<sup>+</sup> cells, at least in part, by enhancing glycolytic processes. Nevertheless, the mechanism of NO-mediated action is not fully understood in the current study and warrants further investigation. It is believed that the NO nanodelivery system will become a precision therapy for reversing aging in the future.

## Methods

### Ethical statement

All animal procedures were conducted in strict compliance with protocols approved by the Ethics Review Committee of Animal Experimentation at Yangzhou University (No. XYLL-2022-169). These procedures were conducted in accordance with the guidelines set forth in the National Institutes of Health's Guide for the Care and Use of Laboratory Animals and in compliance with the principles of the Animal Welfare Act.

### Mice

Male C57BL/6 mice (2 and 20 months) were obtained from Nanjing Cavans Biotechnology Co., Ltd., China. LepR-tdTomato mice were purchased from Cyagen Biotechnology Co., Ltd., China. The mice were housed in a clean room with free access to water and 12 h of light and darkness each day (7 a.m. to 7 p.m.), with a constant temperature of 25 °C.

### Isolation and sorting of LepR<sup>+</sup> cells

The femurs of C57BL/6 mice were collected, and the intact bone marrow was flushed from the femur and subjected to two rounds of enzymatic digestion in medium containing 3 mg mL<sup>-1</sup> type I collagenase (17018029, Gibco), 4 mg mL<sup>-1</sup> neutral protease (4942078001, Roche), and 200 U mL<sup>-1</sup> DNase (89836, Thermo). The enzyme digestion conditions were 15 min each at 37 °C. The digestion was subsequently terminated by the addition of 10 mL of HBSS (14170120, Gibco, Ca/Mg-free) containing 2% FBS and 2 mM EDTA (AM9260G, Invitrogen), and the cells were subsequently resuspended in HBSS buffer (Ca/Mg-free) containing 2% FBS after centrifugation. To sort the LepR<sup>+</sup> cells, the cell suspensions were incubated with a goat anti-LepR-biotin antibody (BAF497, R&D Systems) for 2 h at 4 °C. The cell suspensions were washed three times with staining buffer and incubated with

donkey anti-goat FITC antibody (ab6881, Abcam) for 1 h. The cells were subsequently resuspended in staining buffer and stained with a FACSAria flow cytometer (BD Biosciences) to sort LepR<sup>+</sup> cells for subsequent studies. The gating strategy used for sorting LepR<sup>+</sup> cells is shown in Supplementary Fig. 11.

### Preparation of CB-NPs and CB-LepR

BNN6 (0.75 mg, HY-164117, MedChemExpress), soybean oil (2  $\mu\text{L}$ , S110244, Aladdin), CPPO (1 mg, B101611, Aladdin), and DSPE-PEG-Mal (5 mg, Shanghai ToYongBio Tech Co., Ltd.) were added to 1 mL of tetrahydrofuran (THF, T103263, Aladdin) and mixed uniformly under nitrogen protection. The obtained mixture was subjected to rotary evaporation to remove the solvent and then dried in a vacuum drying oven. The CB-NPs were prepared by adding 1 mL of Milli-Q water to the dried mixture and shaking vigorously.

500  $\mu\text{L}$  of anti-LepR antibody (10  $\mu\text{mol}$ , BAF497, R&D Systems) was mixed with Traut's reagent (200  $\mu\text{mol}$ , I106793, Aladdin) in PBS and reacted at room temperature for 1 h. Excess Traut's reagent was separated via a desalting column. The resulting mixture was added to 1 mL of Milli-Q water containing CB-NPs and mixed thoroughly for 6 h to obtain CB-LepR.

### Characterizations of CB-NPs and CB-LepR

The morphology of the CB-NPs and CB-LepR was observed with a Hitachi HT7800 transmission electron microscope (Hitachi, Tokyo). The composition of the elements was determined via energy dispersive X-ray spectroscopy (EDS, Tecnai G2 F30 S-TWIN). The hydrodynamic dimensions were measured via dynamic light scattering (DLS; Malvern Instruments). High-performance liquid chromatography (HPLC, Dionex system, Thermo Fisher Scientific, Germany) was employed to determine the DLC and DLE of CPPO and BNN6 in CB-NPs. The DLC were calculated via equations from previous studies<sup>56</sup>. Fluorescence images of the nanoparticles were captured via fluorescence microscopy (Carl Zeiss, Axio Imager 2). Flow cytometry analysis was performed with a BD LSRII (BD Bioscience, Heidelberg, Germany). Animal fluorescence imaging was performed on an IVIS spectral imaging system (PerkinElmer).

### H<sub>2</sub>O<sub>2</sub> detection

The  $\text{H}_2\text{O}_2$  level was measured via an  $\text{H}_2\text{O}_2$  probe (Amplex Red, ST010, Beyotime) and an  $\text{H}_2\text{O}_2$  detection kit (S0021, Beyotime) in the femoral marrow cavity of each treatment group (young + PBS, aged + PBS, and aged + CB-LepR). Amplex Red is a fluorescent probe that is highly sensitive to  $\text{H}_2\text{O}_2$  and reacts with  $\text{H}_2\text{O}_2$  to produce an intense red fluorescent substance. It has a maximum excitation wavelength of 571 nm, a maximum emission wavelength of 585 nm, and strong visible absorption at the excitation wavelength, which is detected by absorbance and absorbance at A570. Following 0.5 h of injection into the cavity, the fluorescence intensity of the probe was measured at 570 nm. For the  $\text{H}_2\text{O}_2$  concentration assay, the femoral BM cavity of each group of mice was rinsed and centrifuged to obtain BM supernatant and BM cells, respectively. The BM cells were homogenized with  $\text{H}_2\text{O}_2$  assay lysate and centrifuged at 4 °C to obtain the supernatant, after which the assay reagent was added. Assay reagents were added directly to the BM supernatant. The assay was incubated for 0.5 h at room temperature, and the absorbance at 560 nm was read via an enzyme standardization instrument. A standard curve was drawn using commercial  $\text{H}_2\text{O}_2$ , and the concentration of  $\text{H}_2\text{O}_2$  in the marrow cavity was calculated from the standard curve. LepR<sup>+</sup> and LepR<sup>-</sup> cells were obtained via flow cytometry sorting, and the intracellular  $\text{H}_2\text{O}_2$  concentration was detected as described above.

### Characterizations of NO generation

LepR<sup>+</sup> cells were stained with the NO probe DAF-FM DA (S0019, Beyotime). LepR<sup>+</sup> cells were co-incubated for 24 h with 50  $\mu\text{g}/\text{mL}$



nanopumps in medium containing  $\text{H}_2\text{O}_2$  (0, 50, 100 or 200  $\mu\text{M}$ ). After the supernatant was removed, 1 mL of DAF-FM DA PBS solution (5  $\mu\text{M}$ ) was added, and the mixture was incubated for 20 min at 37 °C after the supernatant was removed. The cells were subsequently washed 3 times with PBS before cell staining was observed under an inverted fluorescence microscope. The above procedure was repeated when  $\text{LepR}^+$  cells were co-incubated with medium containing PBS, CB-NPs,  $\text{H}_2\text{O}_2$  + CB-NPs, or  $\text{H}_2\text{O}_2$  + CB-LepR for 24 h to observe the generation of NO.

The amount of NO produced by the nanopumps in vitro and in vivo was measured via a Griess kit (S0021, Beyotime). For in vitro experiments, nanopumps (50  $\mu\text{g}/\text{mL}$ ) were dispersed in  $\text{H}_2\text{O}_2$  solutions (0, 6.25, 12.5, 25 and 50 mM) in a 37 °C water bath. Then, 50  $\mu\text{L}$  of Griess reagent was added to the supernatant obtained after centrifugation, and the absorbance was measured at 540 nm via a microplate reader. To investigate the in vivo release behavior of NO, the femoral of the young + PBS, aged + PBS and aged + CB-LepR groups were rinsed with PBS at different time intervals (0, 1, and 2 w) to obtain cell suspensions. Then, the  $\text{LepR}^+$  cells were collected via LepR antibody staining and flow cytometry sorting. After the lysis of the  $\text{LepR}^+$  cells, the concentration of NO in the supernatant was determined.

### In vivo imaging

The mice were anesthetized via isoflurane inhalation after  $\text{H}_2\text{O}_2$  probes were injected into the femoral marrow cavities of the young, aged, aged + CB-NPs, and aged + CB-LepR groups for 20 min. The temperature of the imaging chamber was maintained at 30 °C, and the mice were imaged at an excitation wavelength of 570 nm and an emission wavelength of 585 nm.

### Live-cell imaging

After CB-LepR (50  $\mu\text{g}/\text{mL}$ ) was co-cultured with  $\text{LepR}^+$  cells for 24 h, the medium was replaced with fresh medium containing PBS or  $\text{H}_2\text{O}_2$  (200  $\mu\text{M}$ ). After the NO probe (DAF-FM DA, S0019, Beyotime) was added, the cells were imaged by a live-cell analyzer to observe the NO release behavior of CB-LepR. The green fluorescence image of the NO probe was obtained from the FITC channel. Real-time images were acquired at 2 min intervals for 20 min.

### Cytotoxicity of nanopumps

The proliferation of  $\text{LepR}^+$  cells was measured with a Cell Counting Kit-8 (CCK-8, CA1210, Solarbio) and a Live/Dead Staining Kit (CA1630, Solarbio). Briefly, after co-incubation of CB-LepR (0, 50, 100, 150, or 200  $\mu\text{g}/\text{mL}$ ) with  $\text{LepR}^+$  cells ( $1 \times 10^4/\text{mL}$ ) for 24 and 72 h, the medium was replaced with 100  $\mu\text{L}$  of medium and 10  $\mu\text{L}$  of CCK-8 reagent, and the optical density was subsequently measured at 450 nm in a microplate reader (BioTek, VT).  $\text{LepR}^+$  cells ( $1 \times 10^4/\text{mL}$ ) were incubated with different treatment groups for 72 h before the medium was replaced with 200  $\mu\text{L}$  of live/dead staining working solution. After incubation for 30 min at 25 °C in the dark, the cells were imaged with a Zeiss Axiovert 200 fluorescence microscope (Carl Zeiss Inc., Thornwood, NY).

### $\text{LepR}^+$ cells targeting in vivo

NO nanopumps were labeled with CY5.5. Briefly, CY5.5-SH (Shanghai ToYongBio Tech Co., Ltd.) was stirred homogeneously with CB-NPs or CB-LepR overnight in the dark. The mixture was dialyzed in deionized water (molecular weight cutoff = 3 kDa) to remove free CY5.5-SH, resulting in  $\text{CB}^{\text{CY5.5}}$ -NPs and  $\text{CB}^{\text{CY5.5}}$ -LepR. For in vivo targeting, aged mice were euthanized 7 days after the injection of  $\text{CB}^{\text{CY5.5}}$ -NPs or  $\text{CB}^{\text{CY5.5}}$ -LepR into the femoral BM cavity. Femur sections were prepared, and the affinity of the nanomaterial for  $\text{LepR}^+$  cells in the BM cavity was observed via immunofluorescence staining. The antibody used for immunofluorescence staining was anti-LepR-FITC (sc-8391 FITC, Santa Cruz Biotechnology). Furthermore,

cell suspensions were obtained by flushing the marrow cavity at 7 days following the injection of  $\text{CB}^{\text{CY5.5}}$ -NPs or  $\text{CB}^{\text{CY5.5}}$ -LepR into the femoral marrow cavity. The working concentration of the LepR antibody (BAF497, R&D Systems) was thoroughly mixed with the cell suspension and incubated for 2 h at 4 °C in the dark. The cell suspensions were washed three times with staining buffer and incubated with donkey anti-goat FITC antibody (ab6881, Abcam) for 1 h. The cells were then washed with flow cytometry staining solution and analyzed on a flow cytometer. To further validate the targeting of CB-LepR in vivo, NO nanopumps were labeled with FITC-SH (Shanghai ToYongBio Tech Co., Ltd.) to obtain  $\text{CB}^{\text{FITC}}$ -NPs and  $\text{CB}^{\text{FITC}}$ -LepR. PBS,  $\text{CB}^{\text{FITC}}$ -NPs, or  $\text{CB}^{\text{FITC}}$ -LepR were injected into the femoral BM cavity of LepR-tdTomato mice, and the targeting effect of the nanomaterials was detected after 1 week. To investigate the systemic BM targeting properties of CB-LepR, the animals were euthanized at different time points after the intravenous injection of  $\text{CB}^{\text{CY5.5}}$ -LepR into aged mice and the skeleton was thoroughly exposed for fluorescence imaging.

### In vitro aging, osteogenic and adipogenic induction

$\text{LepR}^+$  cells were inoculated in 6-well plates, and cell senescence was observed via SA- $\beta$ -Gal staining (G1580, Solarbio) 7 days after the addition of PBS,  $\text{H}_2\text{O}_2$ , CB-NPs,  $\text{H}_2\text{O}_2$  + CB-NPs,  $\text{H}_2\text{O}_2$  + CB-LepR, or  $\text{H}_2\text{O}_2$  + CB-LepR + 2-DG. Additionally, the cells were cultured with osteogenic induction medium (MUBMX-90041, OriCell) or lipogenic induction medium (MUBMX-90031, OriCell) after cell apposition.  $\text{LepR}^+$  cells were then observed for osteogenesis and adipogenesis at different time intervals after the addition of PBS,  $\text{H}_2\text{O}_2$ , CB-NPs,  $\text{H}_2\text{O}_2$  + CB-NPs, or  $\text{H}_2\text{O}_2$  + CB-LepR. The cells were stained for alkaline phosphatase (ALP, G1480, Solarbio) and alizarin red (ARS, G1452, Solarbio) according to the manufacturer's protocol at 7 and 14 days of induced osteogenic differentiation, respectively. After 21 days of adipogenic induction, the cells were stained with Oil Red O (G1262, Solarbio) according to the manufacturer's protocol.

### In vivo therapeutic efficiency

For local administration, aged mice received femoral intramedullary injections of PBS, CB-NPs, or CB-LepR at a CPPO dose of 5.0 mg/kg. For systemic delivery, PBS, CB-NPs, or CB-LepR were administered via tail vein injection every 2 weeks at the same CPPO dosage (5.0 mg/kg). The femurs were collected after 8 weeks for micro-CT scan analysis. After complete decalcification, 5  $\mu\text{m}$  paraffin sections of the femur were prepared and subsequently stained for immunofluorescence. Positive staining was observed via fluorescence microscopy. The antibodies used for immunofluorescence staining included anti-LepR-biotin (BAF497, R&D Systems), anti-OCN (PA5-78870, Thermo Fisher Scientific), anti-ASL (ab97370, Abcam), anti-P21 (ab188224, Abcam), anti- $\gamma$ -H2AX (ab81299, Abcam), anti-IL-6 (ab290735, Abcam), anti-PERILIPIN (ab316115, Abcam), anti-CD31 (ab222783, Abcam), anti-LYVE1 (ab14917, Abcam), anti-PERIPHERIN (ab246502, Abcam), donkey anti-goat FITC (ab6881, Abcam), and goat anti-rabbit FITC (ab6717, Abcam) antibodies.

### my-HSCs analysis

100  $\mu\text{L}$  of BM cell suspension (concentration of  $1 \times 10^8$  cells/mL) was added to a flow-through tube, Fc receptors were blocked with an anti-CD16/32 antibody (101301, BioLegend) on ice for 20 min, and then, fluorescent antibodies were added to stain the cells on ice protected from light for 1 h. Fluorescent antibodies used for the analysis of my-HSCs (Lineage<sup>+</sup>Sca-1<sup>+</sup>c-Kit<sup>+</sup>(LSK)CD48<sup>+</sup>CD150<sup>high</sup> HSCs) included anti-Lineage Cocktail Isotype Ctrl-FITC (133302, BioLegend), anti-Sca-1-APC (108112, BioLegend), anti-c-Kit-PE/Cyanine7 (105814, BioLegend), anti-CD48-PerCP/Cyanine5.5 (103422, BioLegend), and anti-CD150-PE (162606, BioLegend). The gating strategy used for flow cytometric data is shown in Supplementary Fig. 12.

## RNA sequencing

In vitro and in vivo RNA-seq were conducted by Oebiotech (Shanghai, China) and Majorbio (Shanghai, China), respectively. Briefly, RNA from the PBS, H<sub>2</sub>O<sub>2</sub> and H<sub>2</sub>O<sub>2</sub> + CB-LepR groups was used for in vitro RNA-seq. RNA from LepR cells was sorted from the BM of young + PBS, aged + PBS, and aged + CB-LepR mice for in vivo RNA-seq. The RNA integrity was assessed via an Agilent Bioanalyzer 2100. The RNA-Seq libraries were constructed via an Agilent SureSelect strand-specific RNA library preparation kit and sequenced on a HiSeq 4000 platform (Novogene). A corrected *p* value of 0.05 and log<sub>2</sub> (fold change) were set to 1 as thresholds for significantly differentially expressed genes (DEGs). The groups of DEGs were analyzed for GO, KEGG and GSEA pathway enrichment functions.

## Quantitative RT-PCR

Total RNA was extracted via TRIzol (Vazyme, Nanjing, China) according to the manufacturer's instructions. The RNA concentration was measured with a NanoDrop 2000 (Thermo Fisher Scientific). cDNA was synthesized via a HiScript III RT kit with gDNA wiper (Vazyme, Nanjing, China). qPCR was performed on a QuantStudio3 (Applied Biosystems) with ChamQ Universal SYBR qPCR Master Mix (Vazyme, Nanjing, China). The 2<sup>-ΔΔCt</sup> method was used, and gene expression was normalized to that of Actin. The primers used are listed in Supplementary Table 1.

## Extracellular acidification rate measurements with the Seahorse assay

A total of 1 × 10<sup>7</sup> LepR<sup>+</sup> cells were incubated with PBS, H<sub>2</sub>O<sub>2</sub>, CB-NPs, H<sub>2</sub>O<sub>2</sub> + CB-NPs, or H<sub>2</sub>O<sub>2</sub> + CB-LepR for 24 h. The basal levels of the extracellular acidification rate (ECAR) were then measured on a Seahorse XFe96 Extracellular Flux Analyzer (Agilent Technologies, Santa Clara, CA, USA) according to the XF Glycolytic Stress Test protocol, and glucose (final concentration of 10 mM), oligomycin (final concentration of 1 μM) and 2-DG (final concentration of 50 mM) were sequentially added<sup>53</sup>.

## Micro-CT imaging

The femur was stripped, fixed, and then scanned via micro-CT (Sky-Scan 1176, SkyScan, Aartselaar, Belgium) at an isotropic voxel size of 3.5 μm. A 3D reconstruction was performed via the system software, with the lower-density threshold set to 90. The cylindrical region of interest (ROI) was set at the distal femoral epiphysis, and the trabecular parameters in the ROI were obtained.

## Statistical analysis

Statistical analyses are conducted using GraphPad Prism 9.0 software. The quantitative data were expressed as mean ± SD. Statistical differences were calculated using unpaired student's *t*-test or one-way analysis of variance (ANOVA) when comparing two or multiple groups, respectively. Statistical significance is determined using the following thresholds: \**P* < 0.05; \*\**P* < 0.01; \*\*\**P* < 0.001.

## Reporting summary

Further information on research design is available in the Nature Portfolio Reporting Summary linked to this article.

## Data availability

The RNA-seq data generated in this study have been deposited in the Genome Sequence Archive (GSA) database of the National Genomics Data Center (NGDC) under accession code [CRA025008](https://ngdc.cncr.ac.cn/CRA025008). All data supporting the article are included in the main article, Supplementary Information and the Source Data file. Source data are provided with this article.

## References

- Ambrosi, T. H. et al. Aged skeletal stem cells generate an inflammatory degenerative niche. *Nature* **597**, 256–262 (2021).
- Zhou, B. O., Yue, R., Murphy, M. M., Peyer, J. G. & Morrison, S. J. Leptin-receptor-expressing mesenchymal stromal cells represent the main source of bone formed by adult bone marrow. *Cell Stem Cell* **15**, 154–168 (2014).
- Yue, R., Zhou, B. O., Shimada, I. S., Zhao, Z. & Morrison, S. J. Leptin receptor promotes adipogenesis and reduces osteogenesis by regulating mesenchymal stromal cells in adult bone marrow. *Cell Stem Cell* **18**, 782–796 (2016).
- Gao, X. et al. Leptin receptor(+) cells promote bone marrow innervation and regeneration by synthesizing nerve growth factor. *Nat. Cell Biol.* **25**, 1746–1757 (2023).
- Biswas, L. et al. Lymphatic vessels in bone support regeneration after injury. *Cell* **186**, 382–397.e324 (2023).
- Fang, S. et al. VEGF-C protects the integrity of the bone marrow perivascular niche in mice. *Blood* **136**, 1871–1883 (2020).
- Hominick, D. et al. VEGF-C promotes the development of lymphatics in bone and bone loss. *eLife* **7**, e34323 (2018).
- Mitchell, C. A. et al. Stromal niche inflammation mediated by IL-1 signalling is a targetable driver of haematopoietic ageing. *Nat. Cell Biol.* **25**, 30–41 (2023).
- Verovskaya, E. V., Dellorusso, P. V. & Passegué, E. Losing sense of self and surroundings: hematopoietic stem cell aging and leukemic transformation. *Trends Mol. Med.* **25**, 494–515 (2019).
- Ding, L. & Morrison, S. J. Haematopoietic stem cells and early lymphoid progenitors occupy distinct bone marrow niches. *Nature* **495**, 231–235 (2013).
- Gao, B. et al. Local delivery of tetramethylpyrazine eliminates the senescent phenotype of bone marrow mesenchymal stromal cells and creates an anti-inflammatory and angiogenic environment in aging mice. *Aging Cell* **17**, e12741 (2018).
- Wang, Z., Jin, A., Yang, Z. & Huang, W. Advanced nitric oxide generating nanomedicine for therapeutic applications. *ACS Nano* **17**, 8935–8965 (2023).
- Lundberg, J. O. & Weitzberg, E. Nitric oxide signaling in health and disease. *Cell* **185**, 2853–2878 (2022).
- Mocellin, S., Bronte, V. & Nitti, D. Nitric oxide, a double-edged sword in cancer biology: searching for therapeutic opportunities. *Med. Res. Rev.* **27**, 317–352 (2007).
- Sortino, S. Light-controlled nitric oxide delivering molecular assemblies. *Chem. Soc. Rev.* **39**, 2903–2913 (2010).
- Ye, J. et al. Near-infrared light and upconversion nanoparticle defined nitric oxide-based osteoporosis targeting therapy. *ACS Nano* **15**, 13692–13702 (2021).
- Zuin, M., Rigatelli, G., Scaranello, F. & Roncon, L. Nitrates and osteoporosis: Which relationship?. *Eur. J. Intern. Med.* **43**, e22–e23 (2017).
- Jamal, S. A., Cummings, S. R. & Hawker, G. A. Isosorbide mononitrate increases bone formation and decreases bone resorption in postmenopausal women: a randomized trial. *J. Bone Miner. Res.* **19**, 1512–1517 (2004).
- Rassaf, T. & Kelm, M. Isosorbide-5-mononitrate and endothelial function: a wolf in sheep's clothing. *Eur. Heart J.* **34**, 3173–3174 (2013).
- Hasan, N. et al. Diethylenetriamine/NONOate-doped alginate hydrogel with sustained nitric oxide release and minimal toxicity to accelerate healing of MRSA-infected wounds. *Carbohydr. Polym.* **270**, 118387 (2021).
- Wang, F. S. et al. Nitric oxide donor increases osteoprotegerin production and osteoclastogenesis inhibitory activity in bone marrow stromal cells from ovariectomized rats. *Endocrinology* **145**, 2148–2156 (2004).



22. Lin, Y. J. et al. In situ self-assembling micellar depots that can actively trap and passively release no with long-lasting activity to reverse osteoporosis. *Adv. Mater.* **30**, e1705605 (2018).
23. Zhao, J., Duan, L., Wang, A., Fei, J. & Li, J. Insight into the efficiency of oxygen introduced photodynamic therapy (PDT) and deep PDT against cancers with various assembled nanocarriers. *Wiley Interdiscip. Rev. Nanomed. Nanobiotechnol.* **12**, e1583 (2020).
24. Lerner, S. et al. ASL metabolically regulates tyrosine hydroxylase in the nucleus locus coeruleus. *Cell Rep.* **29**, 2144–2153.e2147 (2019).
25. Stettner, N. et al. Induction of nitric-oxide metabolism in enterocytes alleviates colitis and inflammation-associated colon cancer. *Cell Rep.* **23**, 1962–1976 (2018).
26. Ross, J. B. et al. Depleting myeloid-biased haematopoietic stem cells rejuvenates aged immunity. *Nature* **628**, 162–170 (2024).
27. López-Otín, C., Blasco, M. A., Partridge, L., Serrano, M. & Kroemer, G. Hallmarks of aging: an expanding universe. *Cell* **186**, 243–278 (2023).
28. Ding, J. et al. Self-activatable photo-extracellular vesicle for synergistic trimodal anticancer therapy. *Adv. Mater.* **33**, e2005562 (2021).
29. Li, Y. et al. Imaging of macrophage mitochondria dynamics in vivo reveals cellular activation phenotype for diagnosis. *Theranostics* **10**, 2897–2917 (2020).
30. Gan, Z. et al. Stiffness-tuned and ROS-sensitive hydrogel incorporating complement C5a receptor antagonist modulates antibacterial activity of macrophages for periodontitis treatment. *Bioact. Mater.* **25**, 347–359 (2023).
31. Ceccarini, G. et al. PET imaging of leptin biodistribution and metabolism in rodents and primates. *Cell Metab.* **10**, 148–159 (2009).
32. Mizoguchi, T. et al. Osterix marks distinct waves of primitive and definitive stromal progenitors during bone marrow development. *Dev. Cell* **29**, 340–349 (2014).
33. Chandra, A. & Rajawat, J. Skeletal aging and osteoporosis: cellular senescence and beyond. <https://doi.org/10.20944/preprints202102.0127.v1> (2021).
34. Cheng, M. et al. Age will affect the growth and mineralization ability of the rat osteoblast. *Clin. Lab.* **61**, 899–905 (2015).
35. Liu, X. et al. Oxylipin-PPAR $\gamma$ -initiated adipocyte senescence propagates secondary senescence in the bone marrow. *Cell Metab.* **35**, 667–684.e666 (2023).
36. Li, X. et al. Inflammation and aging: signaling pathways and intervention therapies. *Signal Transduct. Target Ther.* **8**, 239 (2023).
37. Li, C. J. et al. Senescent immune cells release grancalcin to promote skeletal aging. *Cell Metab.* **33**, 1957–1973.e1956 (2021).
38. Yousefzadeh, M. J. et al. An aged immune system drives senescence and ageing of solid organs. *Nature* **594**, 100–105 (2021).
39. Hou, J. et al. Aged bone marrow macrophages drive systemic aging and age-related dysfunction via extracellular vesicle-mediated induction of paracrine senescence. *Nat. Aging* **4**, 1562–1581 (2024).
40. Mi, B. et al. Ageing-related bone and immunity changes: insights into the complex interplay between the skeleton and the immune system. *Bone Res.* **12**, 42 (2024).
41. Ratliff, M., Alter, S., Frasca, D., Blomberg, B. B. & Riley, R. L. In senescence, age-associated B cells secrete TNF $\alpha$  and inhibit the survival of B-cell precursors. *Aging Cell* **12**, 303–311 (2013).
42. Lei, Q. et al. Extracellular vesicles deposit PCNA to rejuvenate aged bone marrow-derived mesenchymal stem cells and slow age-related degeneration. *Sci. Transl. Med.* **13**, eaaz8697 (2021).
43. Yan, P. et al. FOXO3-engineered human ESC-derived vascular cells promote vascular protection and regeneration. *Cell Stem Cell* **24**, 447–461.e448 (2019).
44. Xing, J. et al. Hypoxia induces senescence of bone marrow mesenchymal stem cells via altered gut microbiota. *Nat. Commun.* **9**, 2020 (2018).
45. Yoon, D. S. et al. SIRT1 directly regulates SOX2 to maintain self-renewal and multipotency in bone marrow-derived mesenchymal stem cells. *Stem Cells* **32**, 3219–3231 (2014).
46. Ma, X., Luan, Z., Zhao, Q., Yang, A. & Li, J. NIR-triggered release of nitric oxide by upconversion-based nanoplateforms to enhance osteogenic differentiation of mesenchymal stem cells for osteoporosis therapy. *Biomater. Res.* **28**, 0058 (2024).
47. Pontzer, H. et al. Daily energy expenditure through the human life course. *Science* **373**, 808–812 (2021).
48. Zhao, Z. et al. Body temperature is a more important modulator of lifespan than metabolic rate in two small mammals. *Nat. Metab.* **4**, 320–326 (2022).
49. Roy, D., Perreault, M. & Marette, A. Insulin stimulation of glucose uptake in skeletal muscles and adipose tissues in vivo is NO dependent. *Am. J. Physiol.* **274**, E692–E699 (1998).
50. Stamler, J. S. & Meissner, G. Physiology of nitric oxide in skeletal muscle. *Physiol. Rev.* **81**, 209–237 (2001).
51. Bolaños, J. P., Delgado-Esteban, M., Herrero-Mendez, A., Fernandez-Fernandez, S. & Almeida, A. Regulation of glycolysis and pentose-phosphate pathway by nitric oxide: impact on neuronal survival. *Biochim. Biophys. Acta* **1777**, 789–793 (2008).
52. Lira, V. A. et al. Nitric oxide increases GLUT4 expression and regulates AMPK signaling in skeletal muscle. *Am. J. Physiol. Endocrinol. Metab.* **293**, E1062–E1068 (2007).
53. Jin, Z. et al. Nitric oxide modulates bone anabolism through regulation of osteoblast glycolysis and differentiation. *J. Clin. Invest.* **13**, e138935 (2021).
54. Tanaka, T. et al. Nitric oxide stimulates glucose transport through insulin-independent GLUT4 translocation in 3T3-L1 adipocytes. *Eur. J. Endocrinol.* **149**, 61–67 (2003).
55. McConell, G. K., Rattigan, S., Lee-Young, R. S., Wadley, G. D. & Merry, T. L. Skeletal muscle nitric oxide signaling and exercise: a focus on glucose metabolism. *Am. J. Physiol. Endocrinol. Metab.* **303**, E301–E307 (2012).
56. Zhang, Y. et al. Self-stabilized hyaluronate nanogel for intracellular codelivery of doxorubicin and cisplatin to osteosarcoma. *Adv. Sci.* **5**, 1700821 (2018).

## Acknowledgments

This study was supported by the National Natural Science Foundation of China (82172468 to H.C., 82372436 to H.C. and 32201078 to J.L.); the Outstanding Youth Fund of Jiangsu Province (BK2024047 to H.C.); the Funding for Distinguished Professorship Program of Jiangsu Province and Distinguished Professorship Program of Yangzhou University (137012765 to J.L.); the China Postdoctoral Science Foundation (2023T160553 to H.C.) and the Postgraduate Research & Practice Innovation Program of Jiangsu Province (SJCX22-1819 to K.L.). The authors acknowledge the contribution of Ningbo Freses Information Technology Co., Ltd. in the production of the schematic figures and elements for this article.

## Author contributions

H.C., J.L. and K.L. conceived the study and coordinated the experiments. K.L. performed most of the experiments. S.H. and H.L. contributed to the synthesis of NO nanopumps and RNA-seq data analysis. W.L. and D.Z. participated in the animal modeling, micro-CT scanning and bone parameter analysis. Z.X., C.P., H.W. and D.L. participated in the data analysis. K.L., S.H., and H.L. wrote the manuscript. H.C. and J.L. made constructive suggestions and revised the manuscript. All authors commented on the manuscript.

## Competing interests

The authors declare no competing interest.

## Additional information

**Supplementary information** The online version contains supplementary material available at <https://doi.org/10.1038/s41467-025-61256-5>.

**Correspondence** and requests for materials should be addressed to Jingjing Liu or Hao Chen.

**Peer review information** *Nature Communications* thanks Chang-Jun Li, Jinming Li, and the other, anonymous, reviewer for their contribution to the peer review of this work. A peer review file is available.

**Reprints and permissions information** is available at <http://www.nature.com/reprints>

**Publisher's note** Springer Nature remains neutral with regard to jurisdictional claims in published maps and institutional affiliations.

**Open Access** This article is licensed under a Creative Commons Attribution-NonCommercial-NoDerivatives 4.0 International License, which permits any non-commercial use, sharing, distribution and reproduction in any medium or format, as long as you give appropriate credit to the original author(s) and the source, provide a link to the Creative Commons licence, and indicate if you modified the licensed material. You do not have permission under this licence to share adapted material derived from this article or parts of it. The images or other third party material in this article are included in the article's Creative Commons licence, unless indicated otherwise in a credit line to the material. If material is not included in the article's Creative Commons licence and your intended use is not permitted by statutory regulation or exceeds the permitted use, you will need to obtain permission directly from the copyright holder. To view a copy of this licence, visit <http://creativecommons.org/licenses/by-nc-nd/4.0/>.

© The Author(s) 2025